C. R. Physique 12 (2011) 707–728

Contents lists available at ScienceDirect

Comptes Rendus Physique

www.sciencedirect.com

Ultra cold neutron quantum states / États quantiques des neutrons ultra froids

The GRANIT spectrometer

Le spectromètre GRANIT

Stefan Baessler [a,b], Mathieu Beau [c], Michael Kreuz [c], Vladimir N. Kurlov [d], Valery V. Nesvizhevsky [c,*], Guillaume Pignol [e], Konstantin V. Protasov [e], Francis Vezzu [e], Aleksey Yu. Voronin [f], on behalf of collaborators

[a] *University of Virginia, Charlottesville, VA 22904, USA*
[b] *Oak Ridge Nat. Lab., Oak Ridge, TN 37831, USA*
[c] *ILL, 6 rue Jules Horowitz, Grenoble, F-38042, France*
[d] *ISSP, 2 Institutskaia, Chernogolovka, RU-142432, Russia*
[e] *LPSC/IN2P3-UJF-INPG, 53 rue des Martyrs, Grenoble, F-38026, France*
[f] *Lebedev Institute, 53 Leninskii pr., Moscow, RU-119991, Russia*

ARTICLE INFO

Article history:
Received 17 January 2011
Accepted after revision 11 April 2011
Available online 4 August 2011

Keywords:
Ultra cold neutrons
Quantum mechanics
Gravitation
High-resolution spectroscopy
Extra short-range interactions

Mots-clés :
Neutrons ultra froids
Mécanique quantique
Gravitation
Spectroscopie à haute résolution
Interactions à courte portée

ABSTRACT

The existence of quantum states of matter in a gravitational field was demonstrated recently in the Institut Laue–Langevin (ILL), Grenoble, in a series of experiments with ultra cold neutrons (UCN). UCN in low quantum states is an excellent probe for fundamental physics, in particular for constraining extra short-range forces; as well as a tool in quantum optics and surface physics. The GRANIT is a follow-up project based on a second-generation spectrometer with ultra-high energy resolution, permanently installed in ILL. It has been constructed in framework of an ANR grant; and will become operational in 2011.

RÉSUMÉ

L'existence d'états quantiques de la matière dans un champ gravitationnel a été démontrée récemment à l'Institut Laue–Langevin (ILL), Grenoble, dans une série d'expériences avec des neutrons ultra froids (UCN). Les UCN dans les états quantiques de basse énergie représente une excellente sonde pour la physique fondamentale, en particulier pour contraindre les forces supplémentaires à courte portée, ainsi qu'un outil en optique quantique et en physique des surfaces. Le GRANIT est un projet basé sur d'un spectromètre de deuxième génération avec une ultra-haute résolution en énergie installé en permanence à ILL. Il a été construit dans le cadre d'une subvention de l'ANR, et sera opérationnel en 2011.

1. Introduction

Quantum states of matter should exist in a sufficiently deep and broad potential well of any nature, including gravity. However, gravity is weaker than any other fundamental interaction by many orders of magnitude, so gravitational quantum states of matter had stayed unobserved until very recently. Nevertheless, a decade ago the existence of quantum states

* Corresponding author.
E-mail address: nesvizhevsky@ill.eu (V.V. Nesvizhevsky).

1631-0705/$ – see front matter
doi:10.1016/j.crhy.2011.04.010

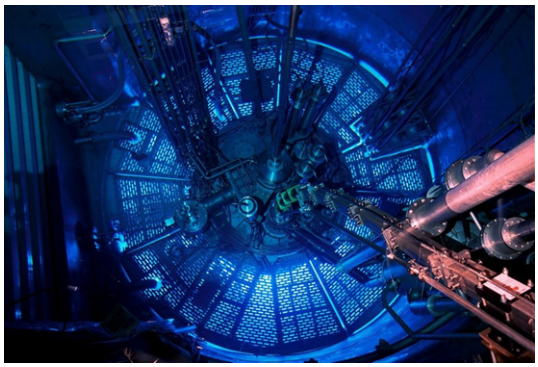

Fig. 1. Top view to the active zone of the ILL high-flux reactor.
Fig. 1. Vue de dessus de la zone active du réacteur ILL à haut flux.

of matter in a gravitational field was demonstrated for the first time in ILL [1] in a series of experiments [2–4] with ultra cold neutrons (UCN) [5–7]. Overviews of these experiments and of physics relevant to this observation could be found in Refs. [8,9]. Serious efforts are devoted to confirm this observation as well as to develop the method of quantum gravitational spectroscopy for various applications (for instance, [10–12] in flow-through mode). The GRANIT is a follow-up project based on a second-generation spectrometer with ultra-high energy resolution (Fig. 1). It will provide more accurate studies of/with gravitational quantum states of UCN, in particular measurements of resonance transitions [12] between them and their interference, in analogy to the neutron whispering gallery phenomenon [13–16]. It will benefit from its permanent installation at the ILL high-flux reactor, from a dedicated ^{4}He UCN source [17] delivering UCN to the GRANIT spectrometer, with no significant dilution of the phase-space density [18,19].

The key property of the GRANIT spectrometer is UCN storage in gravitational bound states for extended periods using a closed specular trap. According to the uncertainty principle, longer observation time provides better defined energy thus higher measurement precision. External perturbations, such as vibrations or gradients and time variations of the magnetic field, have to be minimized. As a fraction of gravitationally bound neutrons is extremely small, we develop neutron detectors with extremely low backgrounds, UCN sources with high phase-space density, and neutron transport systems with low losses [20].

The GRANIT spectrometer will be a unique tool for carrying out a wide range of investigations in fundamental physics, in foundations of quantum mechanics, in surface physics, as well as for development of experimental techniques, for physical modeling and for applications [21–25]. The physical program to be carried out using the GRANIT spectrometer involves a number of scientific institutions from all over the world; also we are open for new ideas and collaborations.

The GRANIT project is being constructed in framework of an ANR (Agence Nationale de la Recherche, France) grant BLANC ANR-05-BLAN-0098-01 received in 2005 by a joint collaboration ILL–LPSC–LMA [26]. Permanent installation of the GRANIT spectrometer at the ILL high-flux reactor is financed by ILL and IN2P3 institutes. Important contributions came from University of Virginia (e.g., through NSF grant PHY-0855610), Petersburg Nuclear Physics Institute, Joint Institute for Nuclear Research and other collaborators.

Infrastructure for the GRANIT spectrometer in ILL is overviewed in Section 2. The GRANIT spectrometer is described in detail in Section 3. The key elements of the GRANIT spectrometer: the mirrors, their production and characterization are presented in Section 4. The method of magnetically-induced transitions between quantum states of UCN in the flow-through mode is developed in Section 5. Feasibility of mechanically-induced transitions between quantum states is commented in Section 6. An option for preparation and analysis of gravitational quantum states in the flow-through mode is given in Section 7. Sapphire crystals are overviewed in Section 8 as a constructing material for UCN experiments. Storage times of UCN in gravitational quantum states are analyzed in Section 9. Theory of interaction of UCN in quantum states with absorber/scatterer is overviewed in Section 10. Finally, transitions between quantum states caused by vibration noise are analyzed in Section 11.

2. Infrastructure for the GRANIT spectrometer in ILL (Michael Kreuz)

First measurements of gravitational quantum states of neutrons were performed using a spectrometer described in Ref. [27]. The spectrometer was temporally installed at PF2 beam position in ILL, the only place where UCN were available at that time. PF2 beam position is located on the upper floor in the reactor building. Compared to this position, permanent installation of the new GRANIT spectrometer (described in more detail in Section 3) at the ground level in the ILL reactor building would bring: (1) higher statistics due to a dedicated UCN source and longer measuring time; (2) lower vibration noise environment (Section 11); (3) clean-room conditions needed to work safely with precision optical components; (4) better magnetic environment (Section 5).

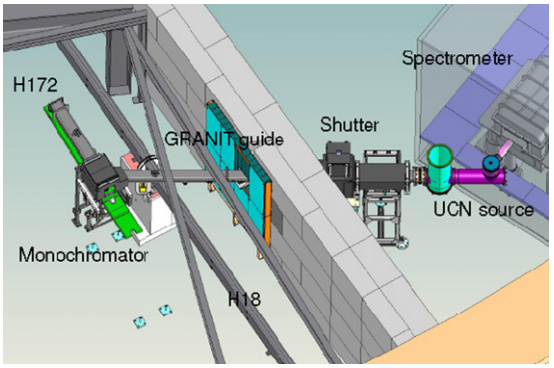

Fig. 2. A scheme of the installation of the GRANIT spectrometer on level C in the ILL reactor.

Fig. 2. Schéma de l'installation du spectromètre GRANIT au niveau C du réacteur de l'ILL.

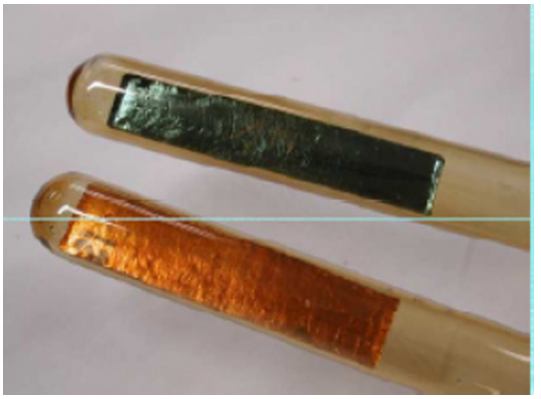

Fig. 3. A plate of normal graphite crystal is shown on top. An analogous plate of graphite crystal intercalated with potassium (thus of a different color) is shown on bottom.

Fig. 3. Plaque de cristal de graphite normale (en haut). Plaque analogue de cristal de graphite intercalé avec du potassium, donc de couleur différente (en bas).

A general scheme of installation of the GRANIT spectrometer is shown in Fig. 2. Cold neutrons with a broad wavelength distribution are delivered from a liquid-deuterium cold neutron source installed in vicinity of the active zone in the ILL high-flux reactor through an H172 neutron guide with a curvature radius of 650 m, a length of 12 m and a cross-section of 8 cm by 8 cm; the guide walls are coated with so-called $m = 2$ super-mirror in order to increase the total number of neutrons delivered to its exit. The last section of this guide (shown in Fig. 2) contains an intercalated-graphite monochromator [28].

Neutrons with a wavelength of 8.9 Å as well as higher-order harmonics are reflected in the intercalated-graphite monochromator towards the GRANIT spectrometer. They are guided through the GRANIT neutron guide with a length of 4.5 m; the guide walls are also coated with $m = 2$ super-mirror. The ^{4}He UCN source is installed downstream a neutron shutter at the exit from this guide. UCN are produced in the source via single-phonon excitation in superfluid ^{4}He and delivered through a special UCN extraction system to the GRANIT spectrometer installed inside a clean room.

A technique to produce intercalated-graphite monochromators has been developed in ILL recently following Refs. [29,30]. In order to reflect neutrons with the wavelength as large as 8.9 Å using Bragg scattering in a crystal, one has to provide increased inter-planner distance that does not exist in nature. This increase is achieved, in our case, by intercalation of mosaic graphite crystals with potassium (K). So-called stage-2 crystals ($C_{24}K$) reflect neutrons with the wavelength 8.9 Å to the take-off angle of 61.2°, as shown in Fig. 2. A plate of normal graphite crystal and a plate of graphite crystal intercalated with potassium are shown in Fig. 3. As production of very large crystals of intercalated graphite is technologically complicated, a monochromator is an assembly of 18 smaller plates aligned relative to each other. The crystals are mounted pair-wise onto graphite bars which are then screwed into an indium sealed aluminum box protecting the crystals from exposure to air, which would destroy the intercalation otherwise. Use of a monochromator and a secondary guide reduces backgrounds with respect to a configuration, in which a converter is placed in a direct neutron beam. The “price to pay” is a reduction in intensity because of imperfections of the monochromator and the secondary guide, and because of omission of multi-phonon processes [31,32], which would contribute to UCN production otherwise.

A photo of the ^{4}He UCN source [17] installed in its position is shown in Fig. 4; the source uses a cryostat previously developed in Munich [33]. The UCN source uses down-scattering of monochromatic cold neutrons with the wavelength of 8.9 Å in superfluid helium via single-phonon excitation [31]. Although the UCN production rate in ^{4}He is very low, produced UCN could be trapped in the production volume due to their nearly total reflection from its walls; thus UCN density would build up. The maximum equilibrium UCN density in a closed helium converter is equal to the product of the production rate density and the neutron storage time. ^{4}He-based UCN sources are usually used in such accumulation mode, with no UCN extraction during the accumulation period. Here we are going to use our source in a quasi-continuous mode. Keeping in mind that extraction of neutrons through an open exit neutron guide decreases UCN storage time in the accumulation volume, we have to limit the extraction slit size, also to extract selectively UCN with very small vertical velocity component needed in the GRANIT spectrometer. Otherwise UCN density in the source would drop down dramatically. A novel method of semi-specular extraction slits has been proposed and tested for this purpose [18,19].

By the beginning of the GRANIT-2010 Workshop, all the infrastructures described above had been produced, assembled and tested. Parameters of the intercalated-graphite monochromators had been improved several times by better adjustments of separate crystal plates forming the monochromator, as well as by replacement of a few crystals of lower quality. Spectrum of cold neutrons deviated by the monochromator had been measured using the time-of-flight method. Cryogenic tests of the ^{4}He UCN source were in progress.

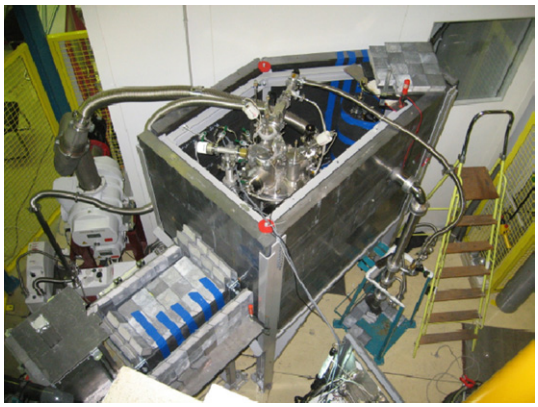

Fig. 4. The ^{4}He GRANIT UCN source installed in front of the clean room.

Fig. 4. La source UCN ^{4}He de GRANIT accolée à la salle blanche.

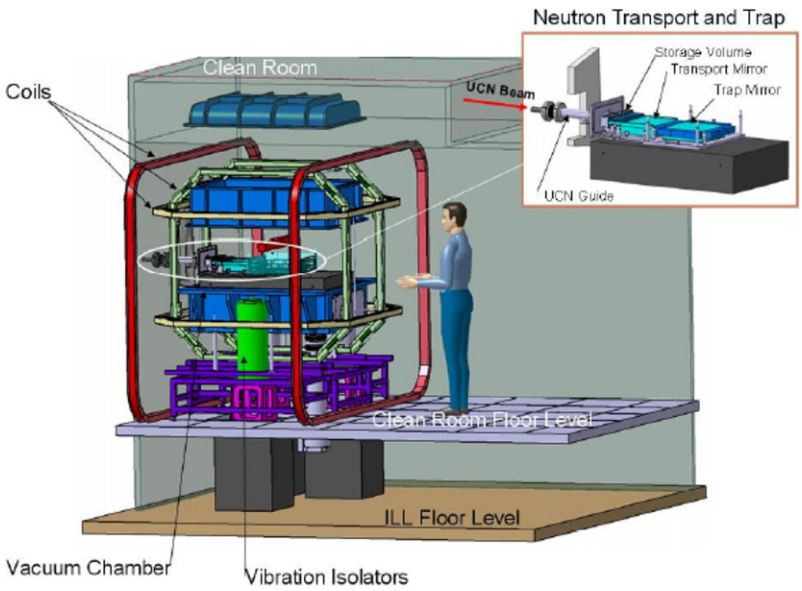

Fig. 5. A general view of the GRANIT spectrometer. The granite table supporting all mirrors and other equipment is shown in the insert.

Fig. 5. Vue générale du spectromètre GRANIT. La table en granit supportant tous les miroirs et autres équipements est représentée dans l'insert.

3. The GRANIT spectrometer (Francis Vezzu)

A general view of the GRANIT spectrometer in its simplest configuration is given in Fig. 5; the optical components are shown in more details in Fig. 6. The spectrometer consists of several neutron-optics elements and UCN detectors installed on a massive granite table in an aluminum vacuum chamber with a volume of $\sim$1.5 m^3: (1) The neutron guide: It connects the spectrometer to the UCN source. A particular design of this guide provides general mechanical flexibility allowing to compensate for eventual misalignments and to decouple the spectrometer from the UCN source vibrations and mechanical stresses. If not suppressed, vibrations would largely decrease UCN storage times in quantum states, and mechanical stresses would not allow precision alignment of neutron optics. An intermediate volume to store UCN is installed at this guide exit. (2) Neutron extraction system: A semi-diffusive narrow slit [18,19] with a height of 100–200 μm allows us to extract UCN with small vertical velocity components needed for the GRANIT spectrometer. Other UCN will be reflected back to the source, thus reducing loss of the UCN density in the source. This configuration allows us to use a ^{4}He UCN source in a flow-through mode. (3) The transport mirror system: To guide UCN from the exit of the semi-diffusive slit to the main mirror, we use a transport system consisting of a horizontal mirror edged by two vertical side walls, and a scatterer/absorber placed above the horizontal mirror. The transport mirror selects a few of the lowest quantum states. Some experiments with gravitational quantum states of neutrons in the flow-through mode could be performed using just this transport mirrors. (4) The neutron mirror: The main optical element of the spectrometer is the trap mirror. It is a 30 cm square mirror sided by four vertical walls coated with DLC (Diamond-Like Carbon) layer. Large size of the mirror trap and high critical

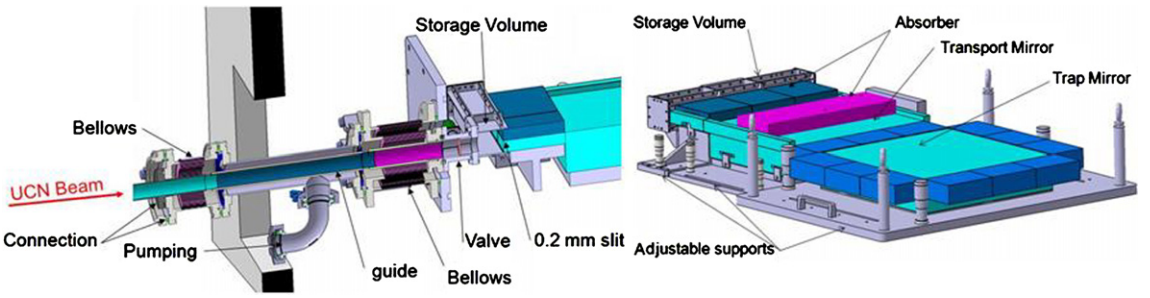

Fig. 6. From the source (left) to the trap (right): UCN guide, UCN valve, intermediate UCN storage, UCN extraction system, UCN storage trap.
Fig. 6. De la source (à gauche) au piège (à droite) : guide UCN, valve UCN, stockage intermédiaire UCN, système d'extraction UCN, piège UCN.

velocity of the DLC coating on side walls are important to increase the number of trapped neutrons. For further detailed description of the mirrors, see Section 4. The mirrors should provide large neutron lifetimes in gravitational quantum states in a storage measuring mode. For the discussion of the factors limiting UCN storage times, see Section 9. As the sensitivity of our experiment is proportional to the neutron lifetime in quantum states, extremely severe geometric characteristics of the mirror should be met, such as the flatness of much better than 1 μm, the roughness of 1 Å, etc. (5) A resonant transition system [12]: For the first experiment in a flow-through mode with the GRANIT spectrometer we will use a magnetic resonant transition system (see Section 5). It consists of a multi-wire assembly installed above the transport mirror; it produces a spatially periodic gradient of the magnetic field. We prefer to avoid the method of mechanical vibrations [21] at this stage as it does not provide precision experiments. (6) Detectors of different type to be used: Three types of detectors will be used at the first stage of the GRANIT experiment. ^{3}He gaseous proportional counters with extremely low background have been developed for this experiment (for more details, see Section 4 in Ref. [20]). They will be used for so-called integral measurements (the total count rate as a function of some parameter, say the height of the split between a mirror and a scatterer). Position-sensitive nuclear-track UCN detectors with a record resolution of $\sim$1 μm [27,4] will be used to study the spatial distribution of neutrons in quantum states (see Section 2 in Ref. [20]). Real-time position-sensitive detectors with a resolution of a few hundred microns will be developed to measure velocity distributions of neutrons in quantum states (see Sections 5 and 6 in Ref. [20]). (7) Numerous spectrum-shaping and spectrum-analyzing devices as well as horizontal leveling and positioning systems will be similar to those used or discussed earlier in Refs. [27,2,3,34,35,4,36,21,37–40]. Their parameters, nevertheless, will be significantly improved compared to the preceding versions.

The GRANIT spectrometer has to be isolated from external perturbations (see, in particular, Section 11). Three main systems have been designed and will be installed around it: (1) An anti-vibration and leveling system. The first level of protection against vibrations, also rough leveling of the installation is provided by three pneumatic feet with controlled valves, which support the vacuum chamber. High precision leveling is provided by three high-load piezo-elements, located in the vacuum chamber under the granite table supporting all the optical elements. These piezo-elements support the granite with all optical elements on top of it. The vibrations associated with ground will be largely suppressed by the system described above. The main residual perturbation is expected to come from the mechanical connection between the GRANIT spectrometer and the UCN source. This effect has to be studied after installation of the spectrometer and the source, and their connection via the neutron guide. One should note that the relative position of all optics elements is not affected by vibrations and slow mechanical drifts anyway, because they are all mounted rigidly to the granite table. (2) The clean room: Optical elements of the GRANIT spectrometer are very sensitive to dust contamination. A precise adjustment with a typical accuracy of 1 μm is required. For this reason, dust particles should be smaller than this value. Moreover, eventual dust particles between two mirror surfaces at such a distance would damage our very delicate and expensive mirrors. Therefore the GRANIT spectrometer is installed inside an ISO 4 clean room (Fig. 7). This clean room is equipped with a laminar air flow coming from its roof and regulated in a way to avoid any turbulence in the central zone of the spectrometer right above the optical elements. (3) The magnetic field control: Compensation of local magnetic fields and introduction of a constant field for the neutron spin guiding are provided by three pairs of coils in Helmholtz configuration, installed around the chamber. The largest one is 3 m large and 2.2 m high. 300 turns of a 2 mm diameter copper wire provide a field of 1.5 mT if the current equals 6.5 Å (see Section 5). Later, for experiments requiring low values of residual magnetic fields, we will replace the coils by a μ-metal anti-magnetic screen.

4. Mirrors for the GRANIT spectrometer, their production and characterization (Stefan Baessler, for Nazario Morgado)

The key element of the GRANIT spectrometer is a set of mirrors to shape/analyze neutron spectra and to store neutrons in quantum states. Here, ongoing efforts are described to produce, select, and characterize the mirrors. In the GRANIT spectrometer, an attempt will be made to store UCN in gravitational bound quantum states to study transitions between them [12]. For the storage, a trap consisting of a bottom mirror, and 12 side mirrors (3 mirrors per a side wall) are foreseen (see Sections 2 and 3 for details). Mirror quality, in particular the geometric shape, surface polishing, purity of the mirrors, and properties of the coatings are of major importance for the efficiency (resolution, precision, count rate, etc.) of the

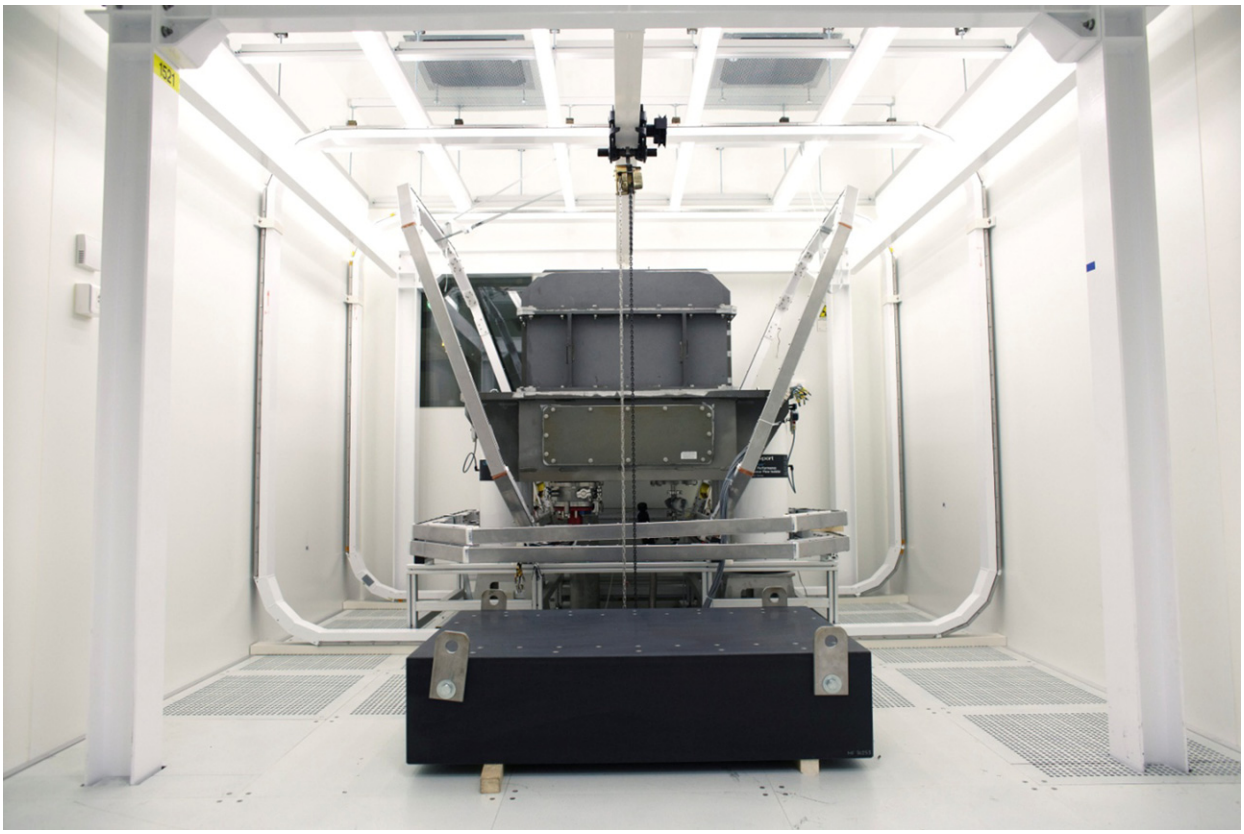

Fig. 7. The GRANIT spectrometer during its assembling inside the clean room.

Fig. 7. Le spectromètre GRANIT lors de son montage à l'intérieur de la salle blanche.

GRANIT spectrometer. Dedicated studies were devoted to optimize and characterize these parameters. Earlier studies of the probability of specular reflection of UCN from small test mirrors (Fig. 8) were published in Refs. [41,42]. It was found that the bottom mirror is best made from uncoated silica. The low critical velocity is not relevant for the bottom mirror. The probability of non-specular reflection, believed to be dominated by the surface roughness, is lowest in this case. The side mirrors (Fig. 9) should be coated with diamond-like carbon (DLC) layer. For the side mirrors, high neutron-optical potential is important, and higher rate of non-specular reflections can be tolerated, however the normal component of UCN velocity in a collision event is much larger than that for collisions with the bottom mirror.

Seventeen uncoated, but shaped and polished silica substrates were acquired from Société Européenne de Systèmes Optiques. Fig. 9 shows the mirror geometry. The dark gray area of the mirror is the relevant surface, which will be in contact with the neutrons. Surface roughness of the uncoated mirrors was measured with an interferometric microscope. The aim for the roughness of the relevant surface was 2 Å (RMS), which was achieved only for some of the samples. The mirror flatness of the relevant surface was measured with a Fizeau interferometer. The average RMS value for the flatness of all mirrors was 16 nm, which is acceptable. The peak-to-peak size of the flatness was, on average, 85 nm, slightly above the goal. In addition, the flatness was measured for the upper surface. The upper surface is relevant only if it is used for transportation of the UCN before or after trapping. The average flatness over that surface was measured to be 120 nm (peak-to-peak), which is acceptable.

The best 12 of the mirrors will be selected for coating and later use. The surface, which is in contact with the neutrons, will receive a coating of DLC with the thickness of 200 nm. This work will be performed using an in-house ion-beam sputtering coater. On 50 mm $\times$ 50 mm $\times$ 10 mm silica samples, the coating procedure was developed and characterized. The first result was that the roughness did not change after coating; it was well below 1 Å for the sample under study. Fig. 10 shows the deformation of the sample mirror due to mechanical stress from the coating.

These results were reproduced in a finite element calculation. The finite element calculation predicts for the bottom mirror that at a thickness of 40 mm, the sag will be 120 nm, which is acceptable. A different possible remedy for the flatness increase due to the coating, which is to coat the back surface in addition, even if that is not needed for the experiment, was not studied. The next steps will be to choose the best of the side mirrors, coat them, and to characterize all mirrors after coating.

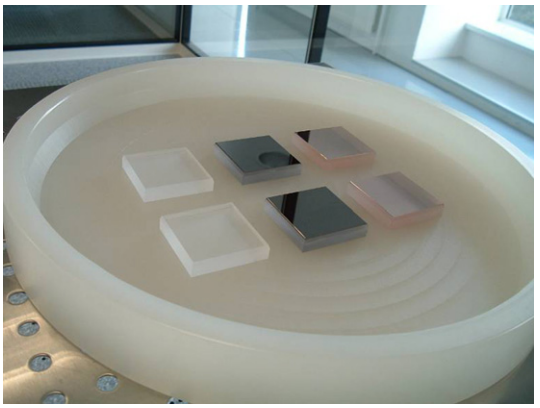

Fig. 8. Small test mirrors with/without coatings (silica, diamond-like and copper coating on silica) prepared in advance to production of the main GRANIT mirrors in order to chose the most suitable substrates and coatings.

Fig. 8. Petits miroirs de test avec ou sans dépôt (silice, diamant et cuivre sur silice) préparés avant la production des miroirs GRANIT principaux, afin de choisir les supports et dépôts les plus appropriés.

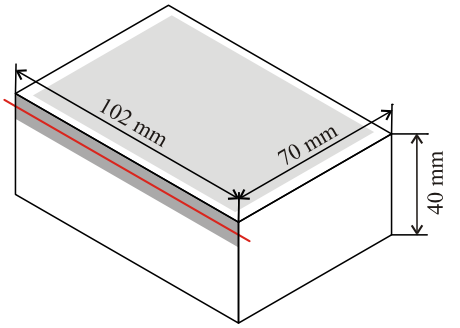

Fig. 9. Side mirror with dimensions. The dark gray area on the left side is the surface which is in contact with the neutrons. Specifications were tested along the red line. The top surface is only relevant if UCN are entering or exiting over this surface; a verifiable specification could only be set for the light gray part of it.

Fig. 9. Miroirs de coté et leurs dimensions. La zone gris foncé sur le coté gauche représente la surface en contact avec les neutrons. Les spécifications ont été testées le long de la ligne rouge. La surface supérieure n'est pertinente que si les UCN entrent ou sortent sur cette surface ; une caractérisation vérifiable est possible uniquement pour la partie grise claire.

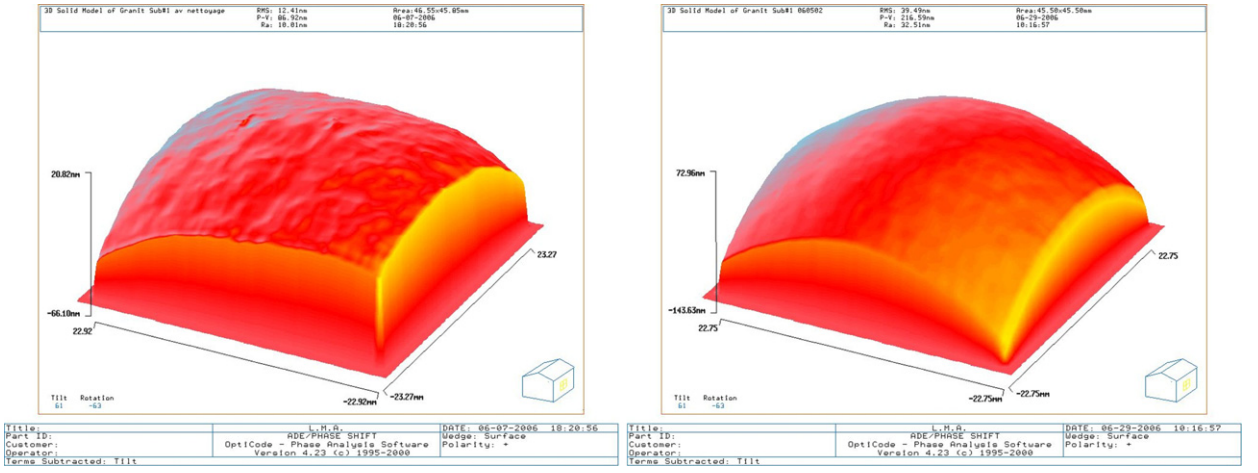

Fig. 10. Flatness profile of a sample, before (left) and after (right) coating with 200 nm DLC. The peak-to-peak size of the flatness was 87 nm before coating, and increased to 217 nm after coating.

Fig. 10. Profil de planéité d'un échantillon, avant (à gauche) et après (à droite) de revêtement DLC de 200 nm. La mesure crête à crête de la planéité était de 87 nm avant le dépôt, et a augmenté à 217 nm après le dépôt.

5. On magnetically-induced transitions between quantum states of neutrons in flow-through mode [12] (Stefan Baessler)

The most convenient method to induce resonant transitions between quantum states, at least at the first stage of our experimental program, is provided by a magnetic field, which varies in space or in time. Here, we describe a scheme, which is intended for first observing resonant transitions between different gravitational quantum states of neutrons in the GRANIT spectrometer. The GRANIT spectrometer (see Section 3) will be used to characterize precisely the gravitationally bound quantum states of UCN by exciting the resonant transitions and performing their spectroscopy [21,43]. Ref. [12] describes a way of detecting resonant transitions in the flow-through mode. The idea is shown and explained in Fig. 11.

The step on the bottom mirror in region (1) of Fig. 11 was already proposed in Ref. [27] as a tool to depopulate the lower quantum states. The one-dimensional quantum states of UCN in the gravitational field above a prefect reflecting mirror are given by $\psi_n(z) \propto Ai((z-z_n)/z_0)$ (for $z>0$), where $Ai(x)$ is the Airy function, $z_0 = (\hbar^2/2m^2g)^{1/3}$ the characteristic length scale, and z_n is the nth solution of $Ai(-z_n/z_0)=0$. In general, neutrons are in mixed states after the step: $\psi(z) = \sum_n c_n \psi_n(z)$. The coefficients c_n are given, in sudden approximation, as:

$$c_n = \sum_l a_l \underbrace{\int \mathrm{d}z\, \psi^*_{in,l}(z)\psi_n(z)}_{Y_{nl}} \tag{1}$$

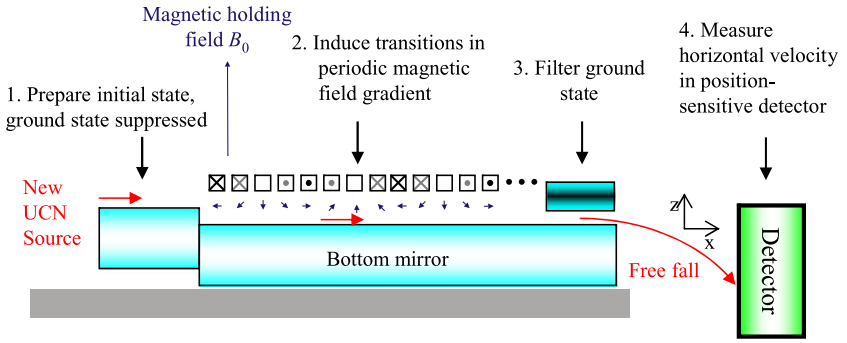

Fig. 11. A setup to detect resonance transitions in a flow-through mode with the GRANIT spectrometer. The setup is optimized in region (1) to provide neutrons mostly in the 3rd quantum state. The magnetic field in the transition region (2) rotates 20 times, each rotation takes $\lambda = 1$ cm. The rotating magnetic field is provided by wires with a current $I_0; 0.7I_0; 0; -0.7I_0; -I_0; -0.7I_0; 0; \ldots$. The filter in region (3) is optimized to transit only the ground state.

Fig. 11. Configuration pour détecter les transitions résonantes dans un mode à flux continu avec le spectromètre GRANIT. La configuration est optimisée dans la région (1) pour fournir des neutrons occupant principalement le troisième état quantique. Le champ magnétique dans la région de transition (2) tourne 20 fois, chaque rotation correspond à $\lambda = 1$ cm. Le champ magnétique tournant est fourni par des fils avec les courants $I_0; 0.7I_0; 0; -0.7I_0; -I_0; -0.7I_0; 0; \ldots$. Le filtre dans la région (3) est optimisé pour la sélection de l'état fondamental.

Table 1
Population of quantum states after step, as a function of the number of a pure incoming state.

Tableau 1
Population des états quantiques après la marche, en fonction du numéro de l'état pur entrant.

Incoming state:	$\psi_{in,1}$		$\psi_{in,2}$		$\psi_{in,3}$	
n (after step)	c_n	$\lvert c_n\rvert^2$	c_n	$\lvert c_n\rvert^2$	c_n	$\lvert c_n\rvert^2$
1	0.040	0.002	−0.027	0.001	0.021	0.001
2	0.325	0.106	−0.166	0.028	0.119	0.014
3	0.766	0.587	−0.141	0.200	0.085	0.007
4	0.527	0.278	0.521	0.272	−0.198	0.039

Here, the incoming neutron is described by the wave function $\psi_{in}(z) = \sum_l a_l \psi_{in,l}(z)$. The basis functions of the quantum states before the step are $\psi_{in,n}(z) \propto \psi_n(z - z_{step})$ (for $z > z_{step}$) given the same wave function, but with an offset $z_{step} =$ 21 μm (the step height). The occupation numbers for the different quantum states after the step are

$$|c_n|^2 = \left| \sum_l a_l Y_{nl} \right|^2 \tag{2}$$

For pure incoming states, the occupation numbers are given in Table 1. The conclusion is that the step populates quantum state 3 (and above) and depopulates quantum state 1.

Let us now discuss the transition region (2), Fig. 11. Here, we have a magnetic field, which consists of a holding field in the z direction ($\vec{B}_0$), and a magnetic field and field gradient that are rotating in the xz plane (see Fig. 11), with a periodicity λ in the x direction. The rotating magnetic field produced by the set of wires above the neutron path is shown in Fig. 12. We neglect a small change of $\beta_z = \partial B_z/\partial z$ with the height z in the following discussion.

The Schrödinger equation is given as

$$H\phi_{k_n,k_y,n} = H_0\phi_{k_n,k_y,n} - \vec{\mu}_n\vec{B}\phi_{k_n,k_y,n} = E\phi_{k_n,k_y,n} \tag{3}$$

To describe solutions, we use basis functions $\phi_{k_n,k_y,n}$, which are a product of the plane wave in the x direction with the wave vector k_n, a plane wave in the y direction with the wave vector k_y, and our one-dimensional basis functions ψ_n used previously. We assume that the magnetic holding field B_0 is sufficiently large thus the neutron spin stays aligned with the z axis.

Without magnetic field, the Hamilton operator of our system H_0 is

$$H_0 = -\frac{\hbar^2}{2m_n}\frac{\partial^2}{\partial x^2} - \frac{\hbar^2}{2m_n}\frac{\partial^2}{\partial y^2} - \frac{\hbar^2}{2m_n}\frac{\partial^2}{\partial z^2} + m_n g z \tag{4}$$

The solutions of the Schrödinger equation without magnetic field are just our basis function above, to a total energy of

$$\frac{\hbar^2 k_n^2}{2m_n} + \frac{\hbar^2 k_y^2}{2m_n} + E_n = E \tag{5}$$

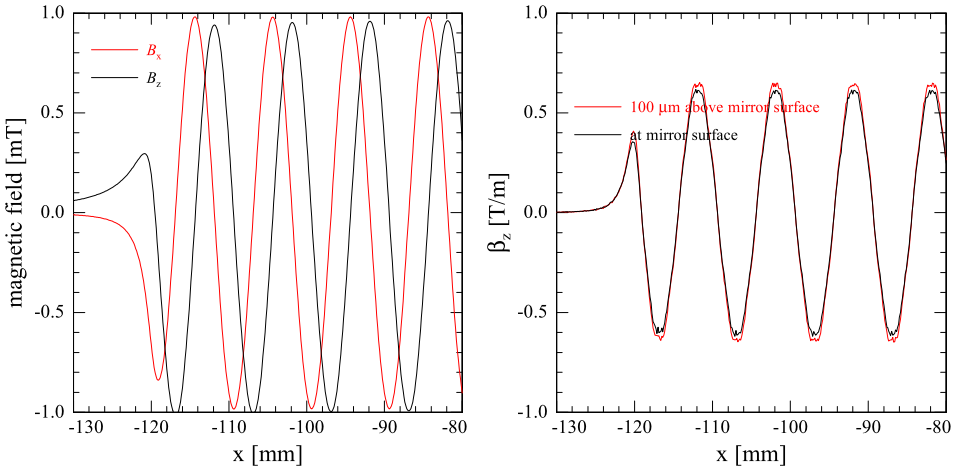

Fig. 12. Magnetic field (B_z and B_x) and the relevant component of the magnetic field gradient $\beta_z = \partial B_z/\partial z$ on the neutron path in region (2). The uniform magnetic holding field is omitted. The center of region (2) is at $x = 0$.

Fig. 12. Champ magnétique (B_z et B_x) et composante pertinente du gradient $\beta_z = \partial B_z/\partial z$ sur le chemin des neutrons dans la région (2). Le champ magnétique uniforme guidant est omis. Le centre de la région (2) est à $x = 0$.

With the magnetic field, we introduce transitions between these basis functions. We still have to conserve energy. The potential $\vec{\mu}_n \vec{B}$ does not depend on the y coordinate, and therefore k_y does not change. Thus, every transition of the z state ($n \to l$) is accompanied by a transition in the x state ($k_n \to k_l$). Note that the energy in the x direction (the first term in Eq. (5), ∼100 neV) is very large compared to the energy in the z direction (the third term, ∼peV).

The rotating magnetic field couples different states of our basis, and we try the ansatz

$$\Phi(x, y, z) = \sum_n a_n(x)\phi_{k_n,k_y,n}(x, y, z) \quad \text{with} \quad \phi_{k_n,k_y,n}(x, y, z) \propto e^{ik_n x + ik_y y}\psi_n(z) \tag{6}$$

We hope for solutions with a slowly varying $a_n(x)$. We plug our ansatz into Eq. (3):

$$\begin{aligned} H\Phi(x, y, z) = {} & \sum_n a_n(x) \underbrace{\left(-\frac{\hbar^2}{2m_n}\frac{\partial^2}{\partial z^2} + m_n g z\right)\phi_{k_n,k_y,n}}_{E_n\phi_{k_n,k_y,n}} - \frac{\hbar^2}{2m_n}\frac{\partial^2}{\partial x^2}\sum_n a_n(x)\phi_{k_n,k_y,n} \\ & \underbrace{-\frac{\hbar^2}{2m_n}\frac{\partial^2}{\partial y^2}\sum_n a_n(x)\phi_{k_n,k_y,n}}_{\frac{\hbar^2 k_y^2}{2m_n}\sum_n a_n(x)\phi_{k_n,k_y,n}} - \sum_n a_n(x)\vec{\mu}_n\vec{B}\phi_{k_n,k_y,n} = \sum_n a_n(x) E\phi_{k_n,k_y,n} \end{aligned} \tag{7}$$

We use Eq. (5) to simplify:

$$-\frac{\hbar^2}{2m_n}\sum_n a_n''(x)\phi_{k_n,k_y,n} - \frac{\hbar^2}{m_n}\sum_n a_n'(x)(ik_n)\phi_{k_n,k_y,n} - \sum_n a_n(x)\vec{\mu}_n\vec{B}\phi_{k_n,k_y,n} = 0 \tag{8}$$

The first term in Eq. (8) can be neglected in comparison to the second term if $a_n(x)$ changes much slower than with k_n. We do that, and multiply with $\phi^*_{k_l,k_y,l}$, and integrate over y and z:

$$\frac{i\hbar^2 k_l}{m_n}a_l'(x) = \sum_n a_n(x)e^{i(k_n - k_l)x}\underbrace{\int \mathrm{d}z\, \psi_l(z)(-\vec{\mu}_n\vec{B})\psi_n(z)}_{M_{nl}} \tag{9}$$

The off-diagonal matrix elements in M_{nl} are responsible for transitions, they vanish for a magnetic field that does not vary along z. An oscillating magnetic field gradient $\beta_z = \partial B_z/\partial z$ induces a transition $n \leftrightarrow l$. This was already shown in Refs. [21,43] in a one-dimensional description.

The difference between k_l and k_n is small:

$$k_n - k_l = \frac{k_n^2 - k_l^2}{k_n + k_l} = -\frac{m_n(E_n - E_l)}{\hbar^2 k_{in}} \tag{10}$$

Table 2
Change of wave vector k_n after transition for a neutron with $k_{in} = k_3$.

Tableau 2
Changement du vecteur d'onde k_n après la transition pour un neutron avec $k_{in} = k_3$.

n	E_n [peV]	$\frac{k_n - k_3}{k_{in}} = -\frac{m_n(E_n - E_3)}{\hbar^2 k_{in}^2}$
1	1.407	7.6×10^{-6}
2	2.460	3.4×10^{-6}
3	3.323	0
4	4.085	-3.0×10^{-6}

where $\hbar k_{in} \approx \hbar k_n \approx \hbar k_l$ is the momentum of the incoming neutron in the xz plane. We show the changes for a neutron initially in state 3 (assuming a neutron velocity along the x axis of $v_x = \hbar k_3/m_n = \hbar k_{in}/m_n = 4.91$ m/s) in Table 2.

Within our planned setup of 20 oscillations of the rotating field, we cannot resolve the change in horizontal velocity of neutrons undergoing transitions between different states n with different k_n. The neutron's expected x position in the lab is well approximated by:

$$x = \frac{\hbar k_{in}}{m_n} t = v_x t \tag{11}$$

We can transform Eq. (9) into a rest frame in which the incoming neutron is not moving along the x axis. The magnetic field gradient in the moving frame is

$$-\vec{\mu}_n \vec{B}(t) = -\mu_n B_0 - \mu_n B_z \cos 2\pi \frac{x(t)}{\lambda} - \mu_n \beta_z z \cos 2\pi \frac{x(t)}{\lambda} = \mu_n B_0 - \mu_n B_z \cos 2\pi \frac{v_x}{\lambda} t - \mu_n \beta_z z \cos 2\pi \frac{v_x}{\lambda} t \tag{12}$$

The oscillation frequency of the magnetic field, as seen by the neutron, is $\omega = 2\pi v_x/\lambda$. Only the third term in Eq. (12) contributes to the off-diagonal elements of the transition matrix M:

$$M_{nl} = \int \mathrm{d}z\, \psi_l(z)(-\vec{\mu}_n \vec{B})\psi_n(z) = -\mu_n \beta_z \cos \omega t \int \mathrm{d}z\, \psi_l(z) z \psi_n(z) \quad \text{for } n \neq l \tag{13}$$

In this frame, the set of equations in [9] is written as

$$i\hbar \frac{k_l}{k_{in}} \dot{a}_l(t) = \sum_n a_n(t) e^{-i(E_n - E_l)t/\hbar} M_{nl} \tag{14}$$

We can neglect the factor k_l/k_{in}. The remaining system of differential equations is usually solved by restricting oneself to a two level system. Here, the transition of interest is $n = 3 \to l = 1$:

$$\begin{aligned} i\hbar \dot{a}_3(t) &= a_1 e^{-i(E_1 - E_3)t/\hbar} M_{13} + a_3 M_{33} \\ i\hbar \dot{a}_1(t) &= a_3 e^{-i(E_3 - E_1)t/\hbar} M_{31} + a_1 M_{11} \end{aligned} \tag{15}$$

With the further approximations that the diagonal elements of the transitions matrix are neglected (no self-coupling), and after keeping only the slow-oscillating terms on the right side of Eq. (15), we get an expression for the transition probability which is well-known from the discussion of Rabi oscillations in atomic physics:

$$p_{3\to1}(t) = \left|a_1(t)\right|^2 = \Omega_{13}^2 \frac{\sin^2(\sqrt{(\omega - \omega_{13})^2 + \Omega_{13}^2} \cdot \frac{t}{2})}{(\omega - \omega_{13})^2 + \Omega_{13}^2} \tag{16}$$

Here we used $\omega_{13} = (E_3 - E_1)/\hbar = 2\pi \cdot 462$ Hz for the resonance frequency of the $3 \to 1$ transition, and $\Omega_{13} = m_n \beta_z \int \mathrm{d}z\, \psi_3(z) z \psi_1(z) = 63.6$ rad/s for the Rabi frequency. Fig. 13 shows the evolution of the transition probability $P_{3\to1}(t)$. Indeed, $a_1(t)$ varies very much slower than the resonance frequency, as assumed above. The figure shows that in order to provide a reasonably high transition probability, we have to select the oscillation frequency of the magnetic field ω at or close to the resonance frequency ω_{13}.

Fig. 14 shows that the resonances are sufficiently small so that different transitions are well separated. This is a necessary condition to be allowed to restrict the discussion to just two gravitational levels in Eq. (15). To improve the resolution considerably, one would have to store the neutrons in their quantum state. Plans for doing so are discussed in Ref. [12].

In region (3), an absorber/scatterer is set at a height of 25 μm and a length of 8 cm. Its function is to let neutrons pass only if they did a transition to the ground state. The properties of this filter are discussed in Ref. [4].

In region (4) in front of the detector, the neutrons fall a distance which depends on their velocity component v_x; therefore, a measurement of the fall height is equivalent to a measurement of the oscillation frequency ω of the magnetic field. The neutrons are detected in a position-sensitive detector. Possible detectors are described in Sections 4–6. Since we use a polychromatic incoming neutron beam, neutrons which hit the detector at different heights experience a wide range

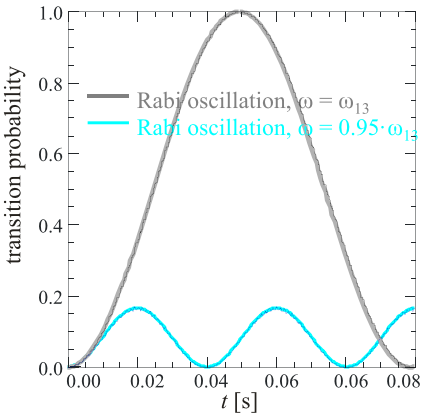

Fig. 13. Transition probability as a function of passage time. The thick lines show the prediction based on Eq. (16). The thin lines show a numerical simulation based on Eq. (15).

Fig. 13. Probabilité de transition en fonction du temps de passage. Les lignes épaisses indiquent les prévisions fondées sur l'Éq. (16). Les lignes minces montrent une simulation numérique basée sur l'Éq. (15).

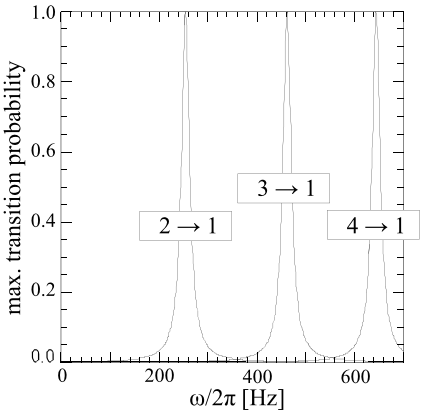

Fig. 14. Maximum transition probability as a function of resonance frequency. The lines show resonance curves for the different transitions in flow-through mode, where the passage time is 0.05 s for a neutron with a speed of $v_x = 4$ m/s.

Fig. 14. Probabilité de transition maximale en fonction de la fréquence de résonance. Les lignes montrent les courbes de résonance pour les différentes transitions dans le mode sans stockage, où le temps de passage est de 0,05 s pour un neutron avec une vitesse de $v_x = 4$ m/s.

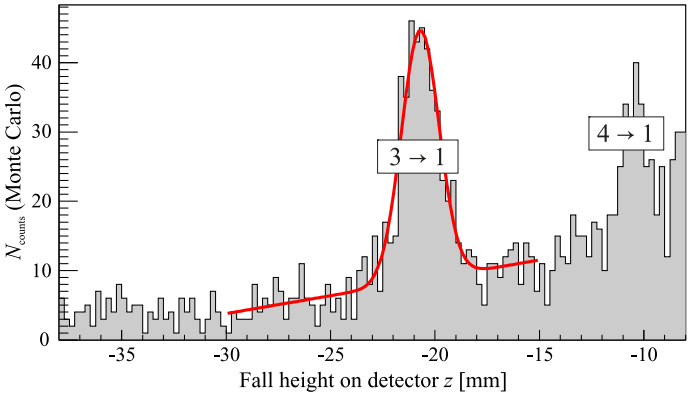

Fig. 15. Simulated result of a flow-through experiment. Shown are the neutron counts as a function of fall height on a position-sensitive detector at the end of region (4). Lower fall height (the right end of the diagram) corresponds to a higher oscillation frequency of the magnetic field ω, as seen by the neutron. From Ref. [44].

Fig. 15. Résultat simulé dans une expérience en mode à flux continu. Le taux de comptage des neutrons dans un détecteur sensible à la position installé à la fin de la région (4) est représenté en fonction de la hauteur de chute. Une hauteur de chute faible (l'extrémité droite de la figure) correspond à une fréquence élevée ω de l'oscillation du champ magnétique vue par les neutrons. Extrait de la Ref. [44].

of oscillation frequencies ω of the magnetic field. We can detect several transitions in a single measurement. However, we have optimum contrast only for the transition for which length of transition region and field strength of the rotating field are optimized.

In Ref. [44], the choice of parameters for the setup described in this paper has been presented. Ref. [44] also contains a simulation of a spectrum obtained with a position-sensitive detector, which is reproduced in Fig. 15. The simulation describes 10 000 neutrons, with a realistic spectrum of the horizontal velocities v_x, which travel through a setup as described in this article. The setup contains a detector with a position resolution of 200 μm and no intrinsic background, a free flight path of 30 cm, and a very high magnetic holding field. 10% of the incoming neutrons are assumed to be in the ground state at the beginning of region (2). Also, the non-perfect suppression of excited states in region (3), and the quantum mechanical spread of the neutron wave function in the free-fall region behind, are included.

A more complete simulation, which includes the motion of the neutron spin, shows that the magnetic holding field needed to neglect the motion of the spin is $B_0 > 30$ mT. It is possible to do the experiment with a smaller magnetic field; we will discuss this in a forthcoming publication.

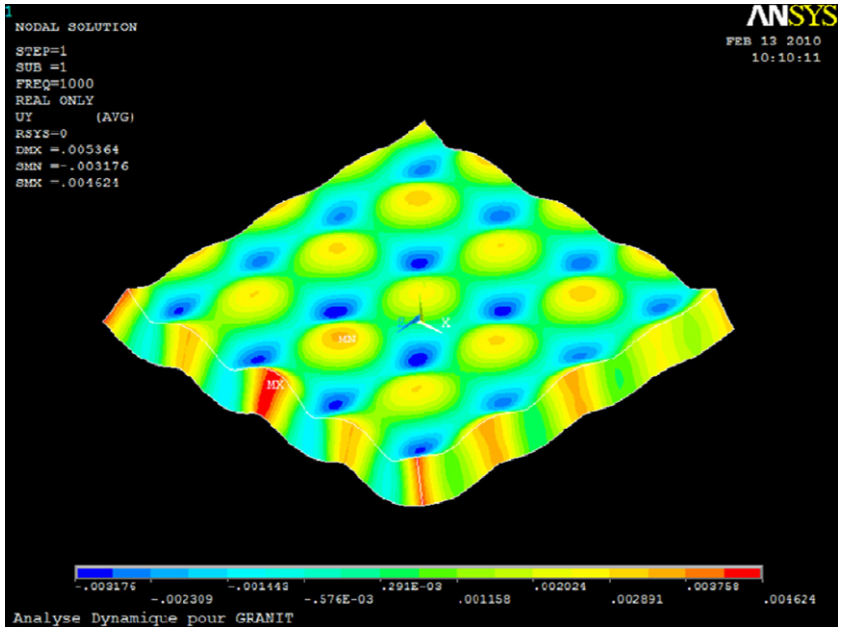

Fig. 16. Surface profile of the silica substrate, excited with 3 piezo-electric actuators (one at the front side and two at the back side) with 1 kHz. The color signifies deformations with a 6 μm peak-to-peak variation.

Fig. 16. Le profil de surface du substrat de silice, excité avec 3 actionneurs piézo-électriques (un à l'avant et deux à l'arrière) à 1 kHz. La couleur indique les déformations, avec une variation de 6 microns crête à crête.

6. On the feasibility of mechanically-induced transitions between quantum states (Stefan Baessler, for Nazario Morgado)

An alternative method to induce transition between quantum states could consist in mechanical oscillations of the mirror with a resonance frequency ([21,44,45], see also Section 11). In order to access feasibility of this method as well as eventual false effects, we will simulate the response of a silica mirror to mechanical vibrations. We assume here that the height of the upper surface of the bottom mirror (below neutrons in gravitationally bound quantum states) can be moved sinusoidally along the vertical axis while keeping the mirror surface horizontal. Possible oscillation frequencies of the upper mirror surface position are between 100 Hz and a couple of kHz, which correspond to the range of values of the transitions between various low gravitational quantum states (see Section 11). The purpose of this study was to verify that the necessary control of the upper mirror surface can be practically achieved.

A silica substrate with the size of the bottom mirror for the GRANIT installation (described in Sections 2 and 3), 30 cm $\times$ 30 cm $\times$ 3 cm were studied in a finite element simulation. The mirror was bonded to 3 piezo-electric actuators, which were positioned at the bottom of the mirrors, and which were assumed to exert a vertical force with the amplitude of 450 N each, and a frequency corresponding to the transition frequency between quantum states. It was attempted to move the upper surface up and down while keeping it horizontal. The results are shown in Figs. 16–18 for three different frequencies.

Furthermore, a different scheme to excite the up–down-movement was simulated, in which the mirror was bonded to 49 regularly spaced piezo-electric actuators below the mirror. In each case, deformation modes of the mirror were excited which led to surface height variations of a couple of μm. The pattern of deformation depended on the excitation frequency. Unfortunately, such a deformation is unacceptable for precision spectrometric studies of gravitationally bound quantum states.

7. Preparation and analysis of gravitational quantum states in a flow-through mode (Mathieu Beau)

After experimental demonstration of existence of the quantum levels of neutrons in the gravitational field of Earth (2), the GRANIT project aims to study precisely the resonant transitions between quantum levels. The previous series of experiments allows extracting the height of the classical turning points at a precision of 12% and 25% for the first and the second quantum levels respectively. The precision was limited by the difficulty to extract information on single quantum states out of an incoherent mixture of them. Here we propose a new theoretical system, see Fig. 19, to prepare a pure eigenstate thus enabling a more accurate determination of the eigenvalues.

The method is designed to resolve spatial features of a single quantum state, in particular the third quantum state $n = 3$. As mentioned, the problem is that the initial flow of neutrons has contributions from different quantum states $n = 1, 2, 3, 4, \ldots$ that compromise accuracy of information on any single state. We therefore suggest a method for the preparation of one quantum state. Our new system has three parts. First, we want to eliminate the lowest quantum states,

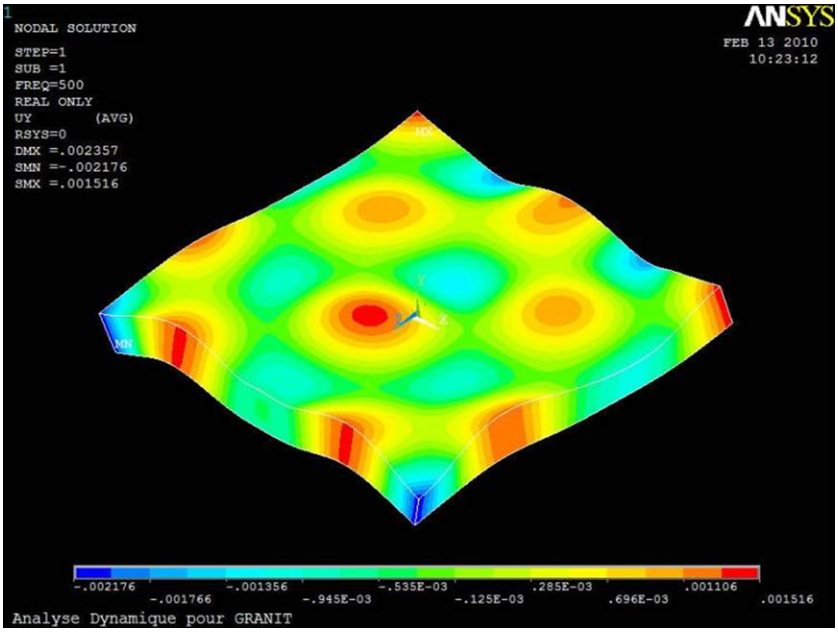

Fig. 17. Simulation as in Fig. 16, but with a frequency of 500 Hz. Here, the peak-to-peak variation of the surface height is 3 μm.

Fig. 17. Simulation comme dans la Fig. 16, mais avec une fréquence de 500 Hz. Ici, la variation crête à crête de la hauteur de la surface est de 3 μm.

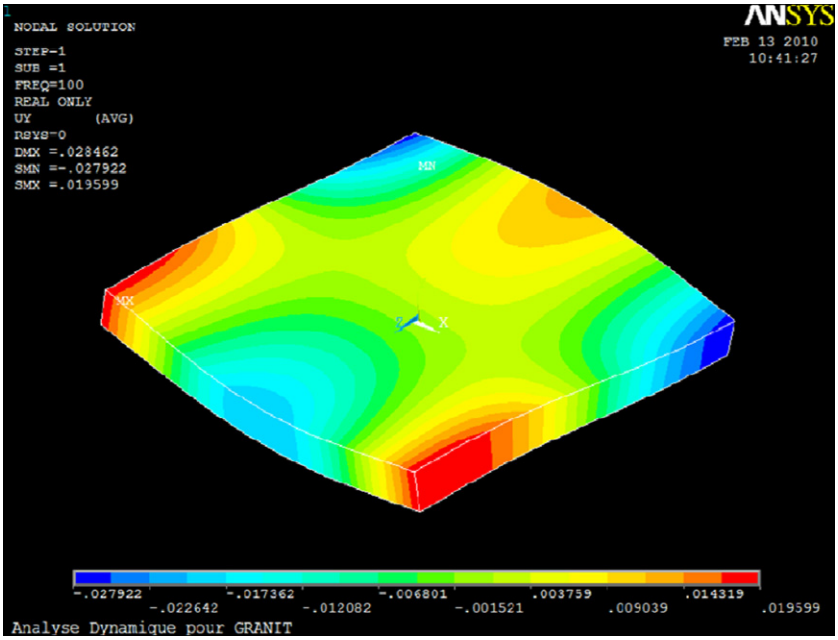

Fig. 18. Simulation like in Fig. 16, but with a frequency of 100 Hz and force amplitude of 45 N per actuator. Here, the peak-to-peak variation of the surface height is 4 μm.

Fig. 18. Simulation comme dans la Fig. 16, mais avec une fréquence de 100 Hz et une amplitude de la force de 45 N par actionneur. Ici, la variation crête à crête de la hauteur de la surface est de 4 μm.

here $n = 1, 2$. Second, we want to eliminate the higher quantum states, here $n = 4, 5, \ldots$ in order to keep only the third quantum state $n = 3$. Third, we analyze the selected quantum state $n = 3$, see Fig. 20.

In Fig. 20, we show how we expect the transmission of neutrons through our system depends on the height z of the slit between the two mirrors in the final step. The slope in the transmission is biggest at around the average height of the 3rd quantum state. There is also some contamination of other steps as seen in the features below $z = 20$ microns. The feature of the curve attributed to the third state might serve to better characterize the third state.

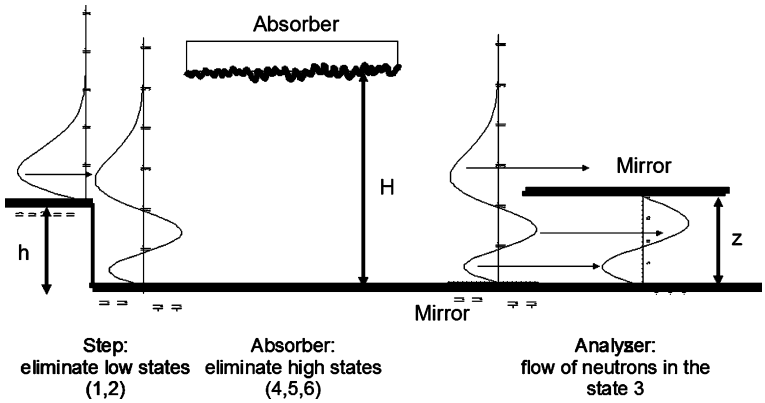

Fig. 19. System to select and analyze a quantum state in a flow-through mode.

Fig. 19. Système pour sélectionner et analyser un état quantique dans un mode à flux continu.

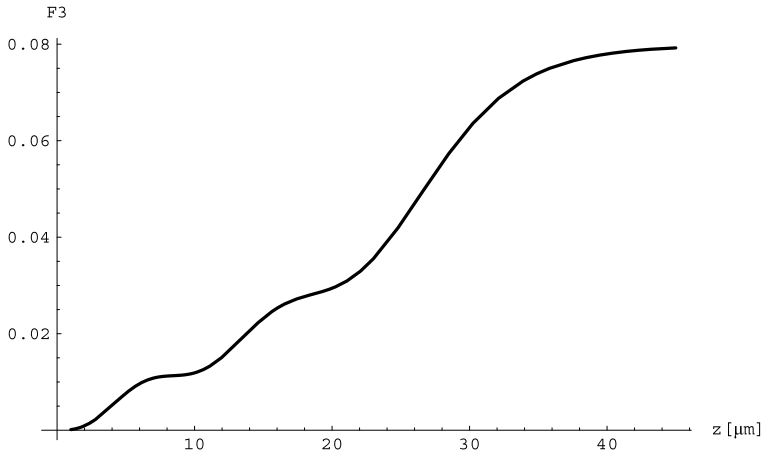

Fig. 20. A sketch showing the expected results from a setup as discussed.

Fig. 20. Un dessin montrant les résultats attendus d'une configuration tel que discuté.

We expect that with this scheme we are able to characterize gravitationally bound quantum states other than the ground state more precisely than it has been done in Ref. [2].

8. Sapphire shaped crystals (Vladimir Kurlov)

Sapphire crystals have been widely used in the GRANIT as well as in related experiments with UCN.

Sapphire has a high refractive index and a broad transmission band spanning the UV, visible and IR bands. Also sapphire has high hardness and melting point, and very good thermal conductivity, tensile strength, and thermal shock resistance. The favorable combination of excellent optical and mechanical properties of sapphire, together with high chemical durability, makes it an attractive structural material for high-technology applications. Frequently, it is the combination of two, or more, of its properties that make sapphire the only material available to solve complex engineering design problems.

The technique of growing sapphire crystals of any predetermined cross-section, constant along the crystal length (rods of various cross-section, ribbons, tubes, fibers, capillaries, rods and ribbons with capillary channels), and crystal with discretely changing cross-sectional configuration (crucibles, boats, near-net-shaped domes, etc.) have been developed, Fig. 21. Since any desired sectional shape can be obtained in the form of ribbons, tubes, rods, and others, cutting processes can be eliminated, allowing for a reduction in cost in comparison with bulk crystals grown by other techniques.

The main applications of shaped sapphire crystals are scanner windows, windows for high-temperature and high-pressure applications, CVD reactors, arc envelopes for vapor lamps, thermocouple sleeves, wear-resistant nozzles, substrates, watch windows, transparent armor, optical systems for high-power laser optics, insulators, high-pressure reactors, high-vacuum equipment, friction moving pieces, guides for textile machine, precision bearings, heat and water impeller meters, chromatograph pistons, engines, domes for high-speed missiles, light guides, acoustic rods, reinforcing elements for composite materials, sensors, nuclear components, research and technological equipment, medicine (implants, scalpels, needles for laser therapy, medical power delivery systems), jewels, etc. [46–48].

Fig. 21. Sapphire shaped crystals.
Fig. 21. Cristaux de saphir de différentes formes.

Sapphire surface provides an excellent tool for *UCN techniques and experiments*.

8.1. Specular reflection of UCN from sapphire surface

It was shown in [42,41] that polished sapphire allows one to efficiently reflect UCN at specular trajectories in realistic experimental conditions. In order to measure so small probability of non-specular reflection, one had even to develop an original measuring technique, based on numerous specular reflections of UCN from two parallel plates placed at very small distances. The typical probability of non-specular reflection for a sapphire surface with $\sim$7 Å roughness and $\sim$1 μm flatness at a distance of 5 cm was $< 2 \times 10^{-3}$; this value could be further improved if needed. However, it is sufficiently low for nearly loss-free UCN transport through a long UCN guide (trap). Although other materials with/without coatings could be used as well in order to provide such specular reflections [49,41], it seems that only sapphire provides a complete set of the properties required. Thus, in contrast to coatings and optical glasses, it survives in severe radiation fluxes in nuclear reactors and in high temperature gradients/variations typical for UCN sources. Its mechanical hardness, in contrast to metals and coatings, allows one to polish its surface to a few angstrom roughnesses and keep it intact in numerous mechanical manipulations. Its effective nuclear potential of 1.5×10^{-7} eV is quite high compared to those for glasses and silicon. Its surface, in contrast to metals and coatings, is free from major contaminations and nanostructures; this is important for providing many UCN reflections needed for their storage.

8.2. Storage of UCN in a sapphire bottle and in a gravitational spectrometer

Low UCN loss in sapphire traps $< 5 \times 10^{-5}$ was proven in experiments [50], where low losses were obtained promptly, without commonly used preliminary cleaning or cooling of surfaces. Even more important, the energy of UCN in a bottle does not change [51], at least the probability of change is $< 10^{-8}$. Until recently, the traditional description of UCN interaction with matter had assumed their loss from closed traps via three channels: their β-decay, their absorption by nuclei in the trap walls, and their inelastic scattering on trap walls. This third possibility assumed the most probable scattering of UCN to the energy range corresponding to the wall temperature; this value exceeds the UCN kinetic energy by five orders of magnitude. However, numerous reports on additional anomalous UCN losses were published, for instance [52]. When studying this puzzle, an additional mechanism for UCN loss from traps was discovered. The UCN energy increased by $\sim 10^{-7}$ eV with the probability of 10^{-8}–10^{-5} per collision [53]; this value exceeded theoretical expectations by orders of magnitude. After such inelastic scattering the UCN might escape from the trap. The small heating of the UCN has been studied over the last years both on solid surfaces (stainless steel, copper, beryllium, etc.) and on liquid surfaces (different kinds of hydrogen-free oils) [53–61]. The experimental discovery of the small heating of UCN required a revision of our theories on the interaction of UCN with a surface [62] and a careful consideration of the different processes at the surface capable of providing inelastic scattering of UCN summarized in Refs. [63,64]: only the scattering of UCN at clusters with a size of $\sim$10 nm can explain the complete set of experimental data obtained; the velocity of the clusters has to correspond to the observed values of energy change. Fig. 22 presents schematic diagram of the UCN gravitational spectrometer used in [51].

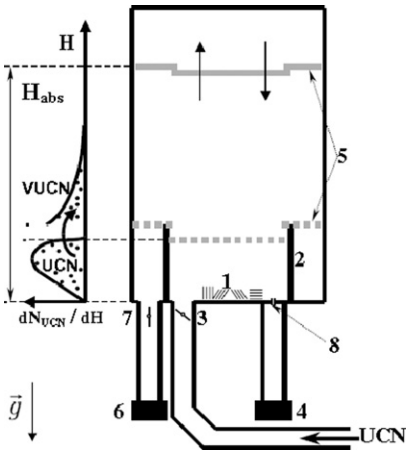

Fig. 22. Schematic diagram of the experimental setup: 1 – sample, 2 – gravitational barrier, 3 – entrance valve, 4 – monitor, 5 – absorber, 6 – detector, 7 – exit valve, 8 – calibration hole.

Fig. 22. Schéma du dispositif expérimental : 1 – l'échantillon, 2 – barrière gravitationnelle, 3 – valve d'entrée, 4 – moniteur, 5 – absorbeur, 6 – détecteur, 7 – vanne de sortie, 8 – trou d'étalonnage.

The principle of its operation can be understood as follows. A typical UCN energy of $\sim 10^{-7}$ eV corresponds to falling down of UCN from the height of ~ 1 m in the Earth's gravitational field; thus UCN motion is strongly affected by gravity. That is why UCN could be confined by the gravitational barrier (2, Fig. 22) and their energy spectrum could be shaped from above by the absorber [5] installed at definite height. If then the energy of the UCN increases by a value compatible to 10^{-7} eV due its interaction with a sample (or with a spectrometer wall) such a UCN might leave the volume confined by the gravitational barrier [2] and could be detected in the neutron detector (6). The probability values of this process on various surfaces ranged from 10^{-5} to 10^{-8} per collision. The set of various measured experimental data indicated that inelastic scattering of UCN on weakly bound nanoparticles at a surface in a state of thermal motion is responsible for the process investigated [65]. These observations, in particular, provide a unique method to study dynamic of nanoparticles and nanostructures, a use hitherto considered impossible. Keeping in mind exceptionally low probabilities of small heating and total losses of UCN in the sapphire surface, as well as large value of its effective nuclear potential and mechanical hardness, one could conclude that sapphire will be the best choice for constructing the principle storage volume of a new advanced gravitational spectrometer analogous to that presented in Fig. 22. The small diameter of this volume feasible in this case, would increase the rate of collisions with sample by one order of magnitude; also it would be perfectly adapted to new compact UCN sources under development [17].

To conclude, various applications of sapphire in UCN physics are rapidly growing during the last few years. Despite the fact that sapphire has been used for many years, it is still in a stage of development. Optimization of standard crystal growth technologies and development of new techniques are actively pursued in order to increase the crystal sizes, improve quality, reduce the cost of material, and to grow complex shapes. There are good reasons to believe that sapphire will be used in a number of new applications.

9. Analysis of storage times of UCN in gravitational quantum states (Guillaume Pignol)

When measuring the energy levels of neutron gravitational quantum states using the resonant transition method, one main parameter is the time T_{pulse} available to excite a given transition. This time T_{pulse} is the time during which an individual neutron is subjected to the periodic excitation interaction and during which a Rabi oscillation between two quantum states occurs. Increasing T_{pulse} will result in two desirable effects. First, the strength of the perturbation needed to complete the transition is lowered. This is definitely a good feature since the perturbation strength is limited by tight instrumental constraints. For example, consider mechanically-induced transitions where the excitation would consist of harmonic oscillation of the bottom mirror: The amplitude of the oscillation is then limited by non-homogeneous deformations in the mirror (see Section 11). Second, the width Δf of the resonance line (the probability of transition as a function of the frequency of the excitation) is narrowed according to the Heisenberg formula $\Delta f = \frac{1}{T_{pulse}}$. Thus, the accuracy for the measurement of the quantum state's spectrum increases with T_{pulse}. This argument gives a minimum T_{pulse} for the resonances to be observed at all. Indeed, the width of a resonance should be smaller than the frequency difference between two neighboring resonances. The condition to resolve the resonances for the few first quantum states is $T_{pulse} > 10$ ms.

In the first phase of the GRANIT project, resonant transitions between gravitational quantum states of UCN will be induced in "flow-through" mode: A neutron will pass one time across a 30 cm long mirror where a periodic magnetic excitation will be applied (see Section 5). In this mode the interaction time will be $T_{pulse} = 50$ ms, long enough to resolve the resonances. In a later stage of the experiment, it is foreseen to increase the interaction time by trapping the neutrons

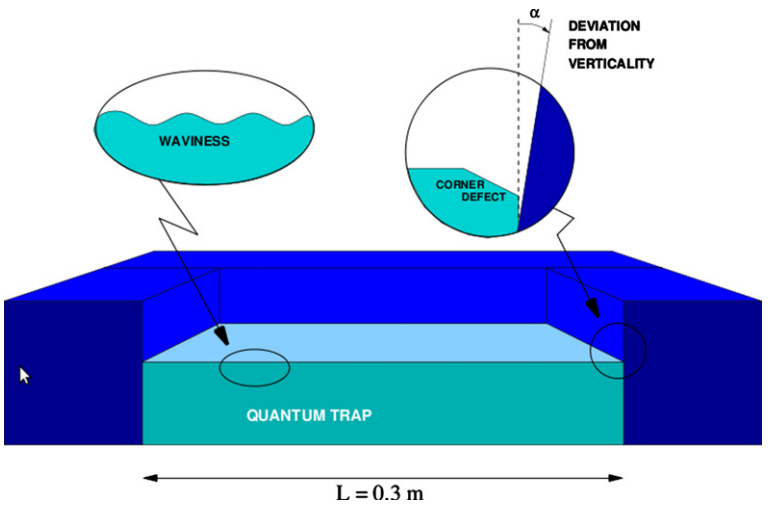

Fig. 23. Scheme of the GRANIT trap with horizontal mirror and side walls.

Fig. 23. Schéma du piège GRANIT avec miroir horizontal et parois latérales.

in quantum states. The trap confines the horizontal motion by means of vertical mirrors on the side of the horizontal main mirror (Fig. 23).

The lifetime of the neutron quantum states in such a trap has been estimated for different relevant sources of loss [66, 44]. One unavoidable loss comes from the beta decay of the neutron itself $T_\beta \approx 880$ s. It constitutes an ultimate limit for the interaction time. Next, not only do we have to consider the disappearance of the neutrons from the trap but also the random transitions from one quantum state to another. Fig. 24 summarizes these estimations, showing the partial lifetimes of the first 10 quantum states. Vibration noise of the bottom mirror is expected to change the energy of the vertical motion of the UCNs, resulting in uncontrolled transition from the initial quantum state to another. This topic is covered in more details in Section 11. Another related loss is caused by waviness of the bottom mirror, which is in some sense equivalent to a vibration in the rest frame of a moving neutron. The loss rate can be calculated within the same formalism. For the numerical estimation the waviness profile of the mirror is taken to be that of mirrors of similar quality and it turns out that the losses due to mirror vibrations as well as mirror waviness are expected to be lower than the beta decay rate.

More critical is the reflection on the vertical walls. Here, some energy transfer between the horizontal and vertical motion is to be feared. The verticality of the side wall is critical and will probably dominate all other sources of losses. For a precision as good as 5×10^{-5} rad, the probability to reflect the first quantum state without loss is 10^{-3} and it gets worse for exited states. It results in a lifetime of the first quantum state of 50 s. This alignment will be done using molecular sticking of the side wall against the side of the horizontal trap. Another difficulty comes from the connection between the horizontal mirror and the vertical side walls. Here a corner defect would constitute a hole into which the UCN fall. Considering a 50 μm long hole, the partial lifetime of the quantum states has been estimated [66,44] to be 40 s, the same for all quantum states.

A completely irrelevant source of loss has also been estimated for academic purpose [67]: the spontaneous decay of an excited state associated to graviton emission. A semi-classical calculation gives a partial lifetime of $T_{decay} = 10^{77}$ s, which is 10^{60} times the age of the universe. Unlike the excited states of atoms, the gravitational quantum states are free of spontaneous decay and are fundamentally stable.

As previously mentioned, the width of the resonance curve for a given transition between quantum states is the inverse of the interaction time T_{pulse} which is in turn limited by the storage time. But for an infinitely long interaction time, other phenomena will limit the resonance width by resonance broadening. The Earth rotation provides such a broadening of the resonance width, via the Coriolis force. Indeed, the neutrons with the horizontal velocity v (East–West component) feel, in addition to gravity, the vertical Coriolis force $F_c = 2mv\Omega\cos(\lambda)$, where λ is the latitude and Ω is the Earth rotation angular frequency. Since the horizontal velocity is distributed from -5 m/s to $+5$ m/s, the effective gravity acceleration is broadened at a relative level of 10^{-4}. This effect results in resonance broadening $\Delta f_{Coriolis}$ (dependent on the state numbers) that cannot be overcome by long interaction time. The time $T_{Coriolis} = \frac{1}{\Delta f_{Coriolis}}$ associated to Coriolis broadening is shown in Fig. 24 by the label “Earth rotation”. It is remarkable that the narrowness of the resonances is not ultimately limited by the beta decay but by the Coriolis force, these limitations are of the same order for the first quantum levels.

In conclusion, one could realistically think of trapping the UCN in quantum states for more than a few seconds. This would represent a two orders of magnitude improvement as compared to the flow-through mode. Equivalently, the UCN should survive 100 collisions on the side walls before a random transition occur. The increase in storage time should translate in narrowed resonance curves, improved accuracy for the transition frequencies and the possibility to measure higher excited levels.

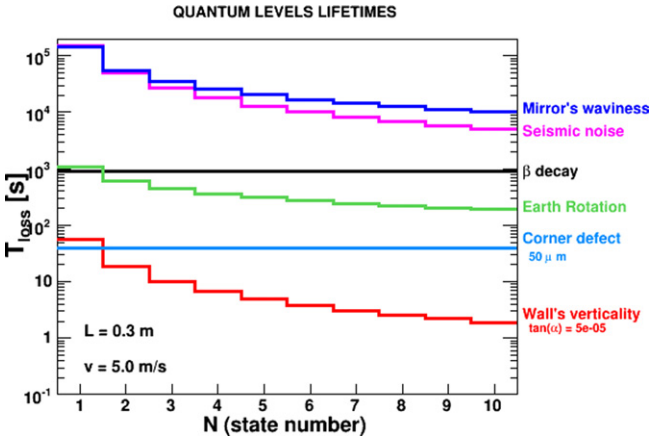

Fig. 24. Estimated lifetime of the first 10 quantum states due to systematic effects discussed in the text.

Fig. 24. Durée de vie estimée des 10 premiers états quantiques dus à des effets systématiques discutés dans le texte.

10. Theory of interaction of UCN in quantum states with absorbers (Alexei Voronin)

The direct observation of the lowest quantum states of neutrons in the Earth's gravitational field above a mirror [2–4, 36] opens an exciting perspective for performing the Equivalence Principle tests in the quantum domain [68,69] as well as short-range fundamental forces studies [70–75], the study of the foundations of quantum mechanics [76–79], surface physics studies [21]. An important ingredient of experiments with neutron gravitational states is initial preparation of the lowest gravitational quantum states. In flow-throw experiments an absorber, placed at a variable height above a perfect mirror, was used for filtering the lowest quantum states. The selective action of absorber on different gravitational states was achieved by adjusting the absorber position above mirror to the neutron gravitational state spatial size. In fact, neutrons in states with the spatial size smaller than the absorber position are weakly affected by the absorber, while those with the spatial size larger than the absorber position are intensively absorbed. The quantitative theory of the absorber interaction with neutrons in gravitational states is important for precision analysis of the experimental data, establishing constraints on resolution of quantum states, for suggesting the effective way of quantum state preparation.

A simple but instructive approach to the theory of neutron–absorber interaction consists in modeling an effect of absorber by means of an optical potential with a negative imaginary part, responsible for absorbing the neutron flux. In such an approach neutron horizontal motion component parallel to the mirror surface is independent from the neutron vertical motion component. The later obeys the Schrödinger equation with the interaction given by superposition of gravitation and optical absorber potential:

$$\left[-\frac{1}{2M}\frac{\mathrm{d}^2}{\mathrm{d}z^2} + Mgz + V(H,z) - \varepsilon_n(H) + i\frac{\Gamma_n(H)}{2}\right]\psi_n(z,H) = 0 \tag{17}$$

Here z is the neutron–mirror surface distance, M is the neutron mass, g is the free-fall acceleration, $V(H,z)$ is the complex optical neutron–absorber potential, which depends on the absorber height H above mirror, $\varepsilon_n - i\frac{\Gamma_n}{2}$ is the complex energy of neutron in the nth gravitational state in presence of an absorber, $\psi_n(z,H)$ is the neutron's wave function in a given state. The neutron states decay due to interaction with an absorber. An important property of such decaying states is that the width $\Gamma_n(H)$ is a rapidly changing function of the absorber height H. A particular form of this function depends on the shape of the absorber optical potential $V(H,z)$. Rather general (and realistic) form of the absorber optical potential has the form:

$$V(H,z) = \frac{V_0 - iW_0}{1 + \exp(\frac{H-z}{\rho})} \tag{18}$$

Here V_0 and W_0 are real and imaginary values of the optical potential, ρ is the diffuseness of the optical potential. It can be shown [37] that in case, when the diffuseness ρ is much smaller than the characteristic gravitational scale $l_0 = \sqrt[3]{\frac{\hbar^2}{2M^2 g}} = 5.87$ μm, $\rho \ll l_0$ and the optical potential depth $V_0 \gg \varepsilon_n$, the absorber properties can be characterized by only one complex valued parameter α, which has a sense of a neutron scattering length on potential $V(H,z)$:

$$\alpha = H - \frac{\hbar}{k} + 2\rho\left(\gamma + \frac{\Gamma'(1+\frac{k\rho}{\hbar})}{\Gamma(1+\frac{k\rho}{\hbar})}\right), \quad k = \sqrt{2M(U_0 - iW_0)} \tag{19}$$

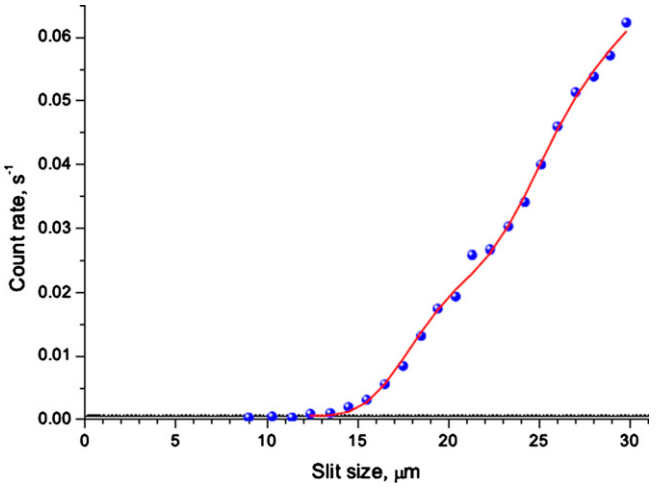

Fig. 25. Neutron count rate at the exit of the waveguide as a function of absorber position. Circles correspond to the experimental data; solid line corresponds to the theoretical fit.

Fig. 25. Taux de comptage de neutrons à la sortie du guide d'onde en fonction de la position de l'absorbeur. Les cercles correspondent aux données expérimentales ; la courbe correspond à l'ajustement théorique.

Here $\Gamma(x)$ is the Gamma-function, and $\gamma = 0.577$ is the Euler constant. We use asymptotic properties of the solutions in linear potential (Airy functions) [80] to get the following expression for the width $\Gamma_n(H)$ [37]:

$$\Gamma_n \approx 2Mg\big|\mathrm{Im}(\alpha)\big|\sqrt{\frac{H-H_n}{H_n}}\exp\left(-\frac{4}{3}\left(\frac{H-H_n}{l_0}\right)^{\frac{3}{2}}\right) \tag{20}$$

Here $H_n \equiv \frac{\varepsilon_n}{Mg}$ has a sense of the spatial size of given gravitational state, the semi-classical expression for H_n, accurate within few percent even for the lowest states is:

$$H_n \approx \left(\frac{3\pi}{4}\left(2n-\frac{1}{2}\right)\right)^{\frac{2}{3}} l_0 \tag{21}$$

The obtained above expression for the width $\Gamma_n(H)$ exhibits very fast decay when the absorber position is greater than the gravitational state spatial size H_n and provides us with quantitative explanation of the selective action of absorber on different gravitational states. The experimental results can be nicely fitted (Fig. 25) by the theoretical curve obtained with the use of the above expression for $\Gamma_n(H)$ (for details see [37]).

The larger the diffuseness of the optical potential ρ, the larger $|\mathrm{Im}(\alpha)|$, and hence more efficient the absorber. Increasing of absorber efficiency is required due to practical limitation of the mirror length and hence the time of state selection by absorber. The practical way to increase ρ is to use absorber with corrugated surface.

The theory of neutron interaction with corrugated surface absorber should include an account of a new phenomenon, namely the effect of non-specular reflections by a rough surface, which results in mixing of the vertical and horizontal components of neutron motion. The theory of neutron transport in the wave-guide with stochastically corrugated surface was developed in [37,81–85,38,39], special case of neutron transport in a corrugated waveguide in the presence of the Earth's gravitational field was studied also in [38,39]. We will follow here the approach developed in [37], which consists in time-dependent treatment of the neutron motion. In such an approach the horizontal motion component is considered classical. The treatment is performed in a frame, moving with the velocity of neutron horizontal velocity component (which can be considered to have given value, as far as horizontal energy is much larger than vertical energy ε_n). The non-specular reflections from rough surface are considered in such a model as transitions between gravitational states in time-dependent neutron–absorber potential $V(H(t), z)$. The time-dependent amplitudes of gravitational states $C_n(t)$ in the suggested model obey the following equation system:

$$\frac{\mathrm{d}C_n(t)}{\mathrm{d}t} = -\frac{\mathrm{d}H_n(t)}{\mathrm{d}t}\sum_{k\neq n} C_k\alpha_{kn}\exp(-iw_{kn}t), \quad \alpha_{kn} = \int_0^\infty \psi_k(H,z)\frac{\partial\psi_n(H,z)}{\partial H}\,\mathrm{d}z \tag{22}$$

Here $w_{kn} = \varepsilon_n - \varepsilon_n$. The above equation system can be solved analytically in particular case of harmonic dependence of the absorber surface height $H(t) = H_0 + b_w\sin(wt)$. Here b_w is the roughness amplitude (corresponding to surface oscillation frequency w in the moving frame). Under additional condition of weak corrugation $b_w \ll l_0$, using the asymptotic properties

Table 3
Frequencies of resonant transitions between quantum states n and k, in Hz.

Tableau 3
Fréquences des transitions de résonance entre les états quantiques n et k, en Hz.

n/k	1	2	3	4	5	6
1	0	254	462	645	813	969
2		0	208	391	559	716
3			0	184	351	508
4				0	168	324
5					0	156

of Airy functions [80] we get the following expression for the effective width of given gravitational state, analogous to the expression for the flat absorber:

$$\Gamma_n \approx Mg\frac{b_w^2}{8|\operatorname{Im}(\alpha)|}\sqrt{\frac{H-H_n}{H_n}}\exp\left(-\frac{4}{3}\left(\frac{H-H_n}{l_0}\right)^{\frac{3}{2}}\right) \tag{23}$$

Here α is the corresponding scattering length on the absorber with uncorrugated *flat* surface. Thus in case of the harmonic profile of the absorber surface we can introduce effective absorber scattering length:

$$\alpha_{eff} = \frac{b_w^2}{16|\operatorname{Im}(\alpha)|} \tag{24}$$

The evident generalization of this result for an arbitrary profile is to substitute the square of roughness amplitude b_w^2 by the sum of squares of the amplitude over all partial frequencies $\langle b^2\rangle = \sum_w b_w^2$. Thus the property of the corrugated surface appears through the *mean roughness amplitude*, which is a sum of partial amplitudes over spectrum of surface oscillations in the moving frame and imaginary part of the scattering length on the flat surface.

Important conclusion of the above analyses is the square dependence of the absorber efficiency on the mean roughness amplitude b^2.

11. Transitions between quantum states caused by vibration noise (Konstantin Protasov)

Various physical effects could destroy our quantum system: non-perpendicularity of the mirror walls, residual magnetic field gradients, etc. In particular, two effects, vibrations and waviness of mirror surfaces, are of vital importance for future experiments. They could be taken into account within the common approach presented in this section.

One can show that the problem of mirror vibrations (stationary Schrödinger equation with a time-dependent boundary condition) and the problem of neutron motion above a wavy mirror (time-dependent Schrödinger equation with stationary boundary condition) are equivalent in the first Born perturbation approximation; thus they can be treated in the same way. These perturbations (vibration and waviness of the mirrors) are considered here as noise. Usually noise is described using so-called noise spectral function, which provides the perturbation intensity as a function of frequency $S(f)$.

We can find a general analytical expression for the probability $p_{n\to k}$ of the transition between two quantum levels n and k. It is proportional to the noise spectrum function: $P_{n\to k} = (\frac{mg}{\hbar})^2 S(f_{nk})$. $S(f_{nk})$ is the value of the spectral function at the frequency of the corresponding transition between two levels. Frequencies of transitions between lowest levels are given in Table 3 (in Hz).

In order to calculate the lifetime of a quantum state, we sum up contributions for all transitions. Namely, for the nth level: $T_n^{-1} = \sum_{n\to k} P_{n\to k}$.

A series of measurements have been performed to characterize the level of vibration noise in the GRANIT spectrometer. We used an accelerometer sensitive in the frequency range from 0 to 500 Hz, precisely the range of interest for the first experiments. A low frequency accelerometer, sensible in the range from 0 to 100 Hz, was also used for consistency checks. It is important to mention that the ILL reactor was on during the measurements, as well as the spectrometer's vacuum pumps. Thus, the measured vibration level is close to realistic experimental conditions, apart from a possible contribution of the UCN source.

Fig. 26 shows the lifetime of neutrons in quantum states for 50 low quantum states measured in standard quite conditions. They are longer that the neutron β-decay lifetime of $\sim$900 s. Effect of large reactor crane operation and human activity around the experimental setup has been investigated as well; they were found to present no concern for stability of the neutron gravitational quantum states. Only deliberate shocks against the apparatus would spoil the experiment. If vibrations exceed temporarily some defined threshold, the measurement will be interrupted. One should note that lifetimes of low states are longer by orders of magnitude than those of excited states. This is explained by higher resonant frequencies for lower states; both the probability of transition and the spectral noise density are low at high frequency. In order to profit from this argument we increased the total weight of our spectrometer by an order of magnitude compared with its previous version; another large improvement consists in much lower vibrations at new position of the GRANIT at the level C of the ILL reactor.

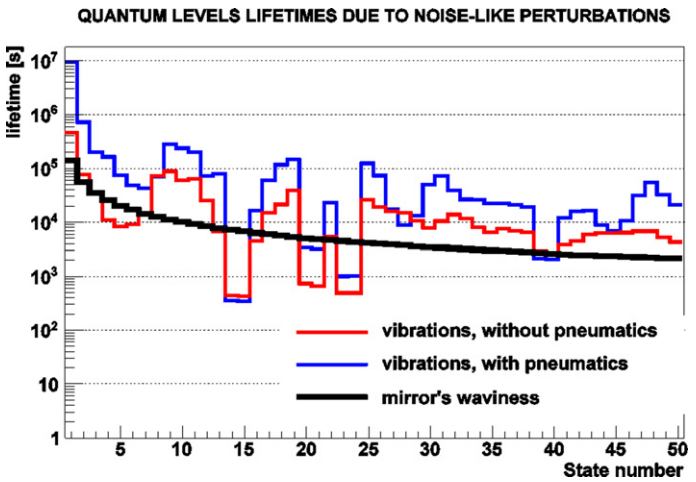

Fig. 26. The partial lifetime of neutrons in a gravitational quantum state as a function of the state number in standard conditions with/without anti-vibration pneumatics are shown with blue and red lines. Black line indicates the estimated partial lifetimes defined by the mirror waviness.

Fig. 26. La durée de vie partielle des neutrons dans un état quantique gravitationnel en fonction du nombre d'états dans des conditions standard avec ou sans système pneumatique anti-vibrations sont représentés par les lignes bleues et rouges. La ligne noire indique la durée de vie partielle définie par l'ondulation de miroir.

This approach can be applied to the problem of the noise induced by waviness of the mirror surface. The only actual problem is that the corresponding spectral function has not yet been measured for future GRANIT mirrors. Nevertheless, it is interesting to evaluate the lifetime of neutrons in quantum states using the spectral function measured with other mirrors with parameters close to those for GRANIT mirror. The result is shown in Fig. 26 by the solid black line. The expected lifetimes are longer than the neutron lifetime as well.

12. Conclusion

In this overview, we describe the recently constructed GRANIT spectrometer designed for measurements of/with gravitational quantum states of neutrons. The spectrometer is permanently installed at the high-flux reactor in the European neutron center Institut Laue–Langevin; we are currently putting it in operation. The spectrometer will be used for a broad range of applications starting from fundamental physics, in particular for constraining extra short-range forces, to quantum optics and surface physics. It will serve primarily for the experimental program of the GRANIT Collaboration; however, it will also be open for so-called "user" experiments.

The works included in this review were supported by grants, BLANC ANR-05-BLAN-0098-01 (France).

References

[1] http://www.ill.eu.
[2] V.V. Nesvizhevsky, et al., Nature 415 (2002) 297.
[3] V.V. Nesvizhevsky, et al., Phys. Rev. D 67 (2003) 102002.
[4] V.V. Nesvizhevsky, et al., Europ. Phys. J. C 40 (2005) 479.
[5] V.I. Luschikov, et al., JETP Lett. 9 (1969) 23.
[6] V.K. Ignatovich, The Physics of Ultracold Neutrons, Clarendon Press, Oxford, UK, 1990.
[7] R. Golub, D.J. Richardson, S.K. Lamoreux, Ultracold Neutrons, Higler, Bristol, 1991.
[8] S. Baessler, Phys. G Nucl. Part. Phys. 36 (2009) 104005.
[9] V.V. Nesvizhevsky, Physics – Uspechi 53 (2010) 645.
[10] T. Sanuki, et al., Nucl. Instrum. Methods A 600 (2009) 657.
[11] T. Jenke, et al., Nucl. Instrum. Methods A 611 (2009) 318.
[12] M. Kreuz, et al., Nucl. Instrum. Methods A 611 (2009) 326.
[13] V.V. Nesvizhevsky, et al., Phys. Rev. A 78 (2008) 033616.
[14] V.V. Nesvizhevsky, et al., Nature Phys. 6 (2010) 114.
[15] V.V. Nesvizhevsky, et al., New J. Phys. 12 (2010) 113050.
[16] V.V. Nesvizhevsky, A.Yu. Voronin, Compt. Rend. Acad. Sci. 12 (2011) 791, doi:10.1016/j.crhy.2011.07.001 (in this issue).
[17] P. Schmidt-Wellenburg, et al., Nucl. Instrum. Methods A 611 (2009) 267.
[18] J. Barnard, et al., Nucl. Instrum. Methods A 591 (2008) 431.
[19] P. Schmidt-Wellenburg, et al., Nucl. Instrum. Methods A 577 (2007) 623.
[20] S. Baessler, A.M. Gagarski, et al., Compt. Rend. Acad. Sci. 12 (2011) 729, doi:10.1016/j.crhy.2011.04.014 (in this issue).
[21] V.V. Nesvizhevsky, K.V. Protasov, Quantum states of neutrons in the earth's gravitational field: state of the art, applications, perspectives, in: Trends in Quantum Gravity Research, Nova Science Publishers, New York, 2006.
[22] S. Baessler, et al., Phys. Rev. D 75 (2007) 075006.
[23] V.V. Nesvizhevsky, et al., Phys. Rev. D 77 (2008) 034020.
[24] A.Yu. Voronin, Phys. Rev. A 83 (2011) 032903.

[25] I. Antoniadis, et al., Compt. Rend. Acad. Sci. 12 (2011) 755, doi:10.1016/j.crhy.2011.05.004 (in this issue).
[26] V.V. Nesvizhevsky, K.V. Protasov, J.M. Mackowski, Project Blanc ANR-05-BLAN-0098-01, 2005–2009.
[27] V.V. Nesvizhevsky, et al., Nucl. Instrum. Methods A 440 (2000) 754.
[28] P. Courtois, et al., Nucl. Instrum. Methods A 634 (2011) 537.
[29] A. Boeuf, et al., Synth. Met. 8 (1983) 307.
[30] C.E.H. Mattoni, et al., Phys. B 344 (2004) 343.
[31] R. Golub, et al., Phys. Lett. A 53 (1975) 133.
[32] C.A. Baker, et al., Phys. Lett. A 308 (2003) 67.
[33] O. Zimmer, et al., Phys. Rev. Lett. 99 (2007) 104801.
[34] V.V. Nesvizhevsky, Usp. Fiz. Nauk 46 (2003) 93.
[35] V.V. Nesvizhevsky, Usp. Fiz. Nauk 47 (2004) 515.
[36] V.V. Nesvizhevsky, et al., J. Res. NIST 110 (2005) 263.
[37] A.Yu. Voronin, et al., Phys. Rev. D 73 (2006) 044029.
[38] A.E. Meyerovich, et al., Phys. Rev. A 73 (2006) 063616.
[39] R. Adhikari, et al., Phys. Rev. A 75 (2007) 063613.
[40] A. Westphal, et al., Europ. Phys. J. C 51 (2007) 367.
[41] V.V. Nesvizhevsky, et al., Nucl. Instrum. Methods A 578 (2007) 435.
[42] V.V. Nesvizhevsky, Nucl. Instrum. Methods A 557 (2006) 576.
[43] G. Pignol, et al., arXiv:0708.2541.
[44] G. Pignol, PhD thesis, University Joseph Fourier, 2009.
[45] H. Abele, et al., Phys. Rev. D 81 (2009) 065019.
[46] V.N. Kurlov, Sapphire: Properties, Growths and Applications, Elsevier Science Ltd, ISBN 0-08-0431526, 2001, p. 8259.
[47] V.N. Kurlov, S.N. Rossolenko, N.V. Abrosimov, Kh. Lebbou, Shaped Crystal Growth, John Wiley and Sons, ISBN 978-0-470-71244-3, 2010, pp. 257–354.
[48] E.R. Dobrovinskaya, L.A. Lytvynov, V. Pishchik, Sapphire: Materials, Manufacturing, Applications, Springer, ISBN 0387856943, 2009, p. 3.
[49] Ch. Plonka, et al., Nucl. Instrum. Methods A 578 (2007) 450.
[50] Grenoble: ILL experimental report TEST-691, 2004.
[51] D.G. Kartashov, et al., Int. J. Nanosci. 6 (2007) 501.
[52] V.P. Alfimenkov, et al., JETP Lett. 55 (1992) 84.
[53] V.V. Nesvizhevsky, et al., Europ. J. Appl. Phys. 6 (1999) 151.
[54] V.V. Nesvizhevsky, et al., Phys. At. Nucl. 62 (1999) 776.
[55] L. Bondarenko, et al., JETP Lett. 68 (1998) 691.
[56] A.V. Strelkov, et al., Nucl. Instrum. Methods A 440 (2000) 695.
[57] L. Bondarenko, et al., Phys. At. Nucl. 65 (2002) 11.
[58] E.V. Lychagin, et al., Phys. At. Nucl. 63 (2000) 609.
[59] A.P. Serebrov, et al., Phys. Lett. A 309 (2003) 218.
[60] E.V. Lychagin, et al., Phys. At. Nucl. 65 (2002) 1995.
[61] A. Steyerl, Europ. Phys. J. B 28 (2002) 299.
[62] A.L. Barabanov, et al., Europ. Phys. J. B 15 (2000) 59.
[63] M. Utsuro, et al., Nucl. Instrum. Methods A 440 (2000) 709.
[64] V.V. Nesvizhevsky, Phys. At. Nucl. 65 (2002) 400.
[65] E.V. Lychagin, et al., Nucl. Instrum. Methods A 611 (2009) 302.
[66] V.V. Nesvizhevsky, et al., arXiv:0708.2541, 2007.
[67] G. Pignol, et al., Class. Quant. Grav. 24 (2007) 2439.
[68] R. Aldrovandi, et al., arXiv:gr-qc/0212034, 2002.
[69] A. Herdegen, et al., arXiv:gr-qc/0110021, 2003.
[70] H. Murayama, et al., Phys. Rev. D 66 (2002) 344.
[71] O. Bertolami, et al., Phys. Rev. D 72 (2005) 025010.
[72] R. Onofrio, et al., Phys. Rev. D 55 (1997) 455.
[73] E. Narevicius, et al., Europ. Phys. Lett. 62 (2003) 789.
[74] V.V. Nesvizhevsky, et al., Class. Quant. Grav. 21 (2004) 4557.
[75] V.V. Nesvizhevsky, et al., J. Res. NIST 110 (2005) 269.
[76] N.E. Mavromatos, arXiv:gr-qc/0407005, 2004.
[77] R.W. Robinett, Phys. Rep. 392 (2004) 1.
[78] J.T. Bowles, Nature 415 (2002) 267.
[79] B. Schwarzschild, Phys. Today 55 (2002) 20.
[80] M. Abramowitz, I.E. Stegun, Handbook of Mathematical Functions, Dover Publ., New York, 1965.
[81] S.K. Sinha, et al., Phys. Rev. B 38 (1988) 2297.
[82] R. Pynn, Phys. Rev. B 45 (1992) 602.
[83] J.A. Sanchez-Gil, et al., Phys. Rev. B 59 (1999) 5915.
[84] N.M. Makarov, et al., Phys. Rev. B 60 (1999) 258.
[85] A.E. Meyerovich, et al., Phys. Rev. B 60 (1999) 9129.